

Spectral Characterization of Two-Dimensional Photonic Crystal Slabs by Using Midinfrared Angle-Resolved Reflection Measurement

シティ, ハリマ

<https://hdl.handle.net/2324/6758955>

出版情報 : Kyushu University, 2022, 博士 (工学), 課程博士
バージョン :
権利関係 :

Spectral Characterization of Two-Dimensional
Photonic Crystal Slabs by Using Midinfrared
Angle-Resolved Reflection Measurement

角度分解反射測定による2次元フォトリック
結晶スラブのスペクトル評価

Siti Chalimah

Department of Chemistry and Biochemistry
Graduate School of Engineering
Kyushu University

August 2022

Table of Contents

Chapter 1	Introduction	1
1.1	Scientific backgrounds	1
1.1.1	Principle of quantum cascade lasers.....	1
1.1.2	Optical cavity design	3
1.1.3	Photonic crystals.....	4
1.1.4	Photonic band structure	4
1.1.5	Quality factor.....	6
1.2	Previous works	8
1.2.1	Progress in photonic crystal surface emitting lasers (PCSELS)	8
1.2.2	Surface emitting quantum cascade lasers	8
1.3	Remaining challenges	9
1.3.1	Characterization technique for photonic band structures in the midinfrared region.....	9
1.3.2	Photonic band structures in laser devices.....	9
1.4	Outline of the thesis.....	9
Chapter 2	Method for high-precision angle-resolved measurement in the midinfrared region.....	15
2.1	Introduction	15
2.2	Design and installation	16
2.3	Test performance	18
2.3.1	Estimation of angle resolution.....	18
2.3.2	Midinfrared characterization of photonic crystal slabs	19
2.4	Conclusion.....	22
Chapter 3	Symmetry assignment and formation of Dirac cones materialized by effective degeneracy.....	25
3.1	Introduction	25
3.2	Methods	25
3.2.1	Sample fabrication.....	25
3.2.2	Angle-resolved reflection measurement.....	26
3.2.3	Theory.....	27
3.3	Results and discussions	28
3.3.1	Angle-resolved reflection spectra.....	28
3.4	Conclusion.....	34
Chapter 4	C_{4v} -symmetry photonic crystal slabs for application to photonic crystal surface-emitting quantum-cascade lasers	36
4.1	Introduction	36
4.2	Methods	36
4.2.1	Samples.....	36
4.2.2	Angle-resolved reflection measurement.....	36
4.2.3	Theory.....	37
4.3	Results and Discussions	40
4.3.1	Midinfrared characterization of PC slabs	40
4.3.2	Mode assignment and dispersion relations.....	42
4.3.3	Q-factor quantification	43
4.4	Conclusion.....	46
Chapter 5	Photonic crystal slabs with different pillar shapes and filling factors for application to photonic crystal surface-emitting quantum-cascade lasers	48
5.1	Introduction	48

5.2	Methods	48
5.2.1	Design.....	48
5.2.2	Samples.....	49
5.2.3	Optical measurement	49
5.3	Results and Discussions	50
5.3.1	Reflection spectra at normal incidence.....	50
5.3.2	Angle-resolved reflection spectra and dispersion relation	54
5.4	Conclusion.....	56
Chapter 6	Summary and outlook.....	58

Chapter 1 Introduction

1.1 Scientific backgrounds

1.1.1 Principle of quantum cascade lasers

Quantum cascade lasers (QCLs) are known as semiconductor lasers based on intersubband transitions [1.1,2]. The mechanism of light emission in QCLs differs from that of conventional semiconductor lasers based on interband transitions. For lasers with interband transitions, photon emission occurs with the recombination of an electron in the conduction band and a hole in the valence band. In contrast, for lasers with intersubband transitions, photon emission occurs when an electron transits between subbands either in the conduction band or in the valence band. Thus, the emission wavelength can be controlled by tailoring quantum-well thickness.

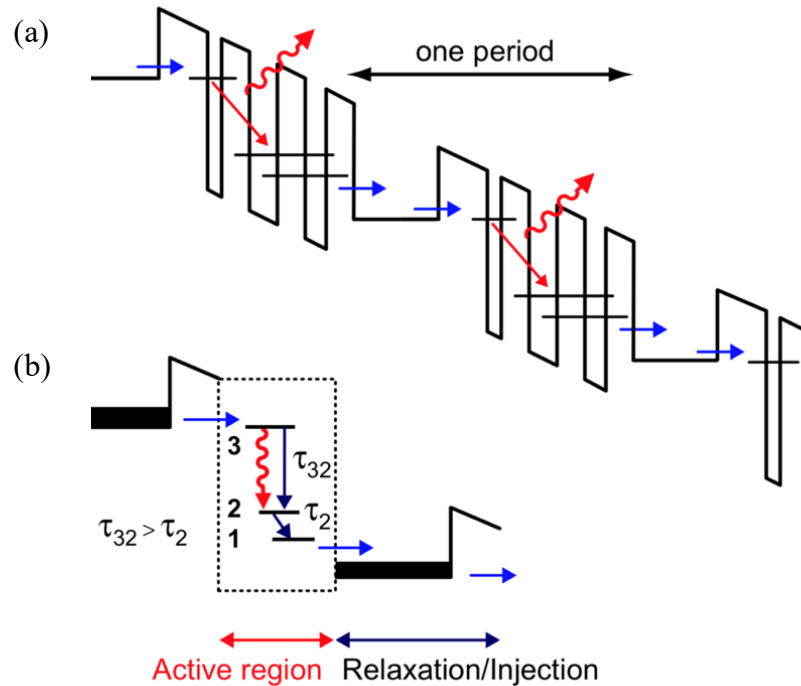


Figure 1.1. (a) Schematic diagram of the conduction band diagram of QCLs. (b) A three-level laser design for QCLs [1.3].

Figure 1.1 shows the example of the QCL structure that consists of the active region and the relaxation/injection region. In this case, the active region has a three-level system. To achieve population inversion, the lifetime for electrons to transit from level 3 to 2 is longer than that from level 2 to 1. After the optical transition, electrons stay in the relaxation/injection region, and then get injected to the next period via resonant tunneling.

The history of semiconductor lasers was triggered by the operation of a homojunction semiconductor laser in 1964. Afterward, the laser technology has rapidly been developed because they can realize compact devices. However, early semiconductor lasers worked only at cryogenic temperatures and in pulsed laser operation. To address these problems, Alferov *et al.* invented heterostructure semiconductor lasers. They are composed of multiple semiconductors that have different bandgap energies [1.4–6].

After the invention of heterostructure semiconductors, Esaki proposed semiconductor superlattices comprising periodically alternating two semiconductors, i.e., wells and barriers. In superlattices, the energy band splits into several minibands, in which optical transitions are possible to occur either in the conduction band or in the valence band. Superlattice structures were successfully applied to QCL, which was demonstrated for the first time by Faist, Capasso, Sivco, Sirtori, Hutchinson, and Cho in 1994 [1.1]. They grew InGaAs/AlInAs material systems, which are lattice matched to InP. The laser emitted light at a wavelength of 4.2 μm at maximum temperature of 90 K.

Accordingly, QCLs have tremendously been developed because they can cover broad spectral emission at midinfrared wavelengths from 3 to 20 μm [1.1, and 1.7–11]. In this spectral range, we can observe the rotational absorption peaks of various kinds of harmful and toxic gases such as nitrogen monoxide (NO), carbon monoxide (CO), and carbon dioxide (CO₂), as shown in Fig. 1.2. Therefore, QCL is regarded as one of the most promising laser candidates for gas sensing and analysis [1.12–16].

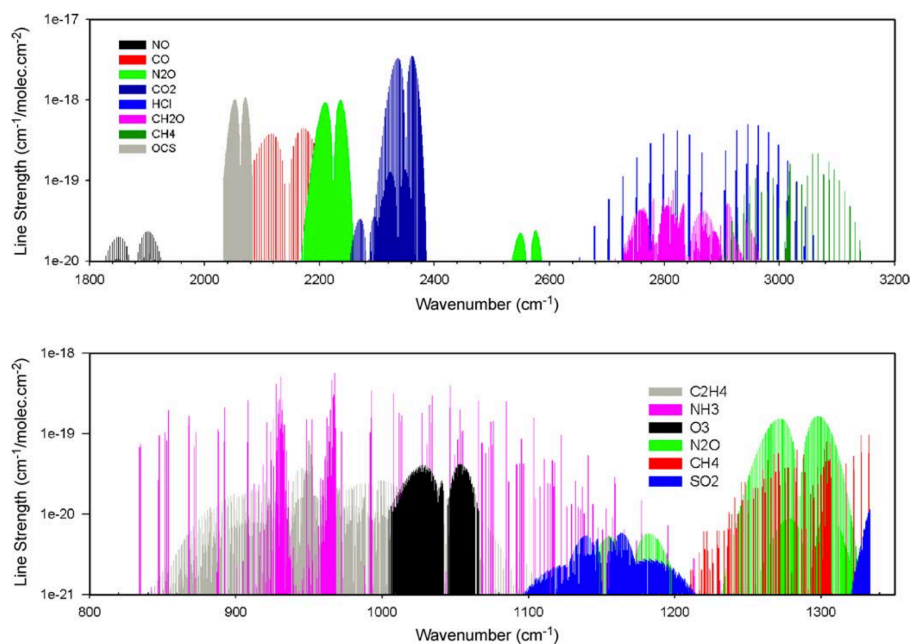


Figure 1.2. The absorption peak simulated with HITRAN. Adopted from [1.13].

1.1.2 Optical cavity design

Optical feedback occurs when the active region is put inside an optical cavity. There are two typical architectures for semiconductor lasers, as shown in Fig. 1.3, namely, edge emitting lasers (EELs) [1.17–19] and vertical cavity surface emitting lasers (VCSELs) [1.20–22]. The EELs emit light in the in-plane direction (parallel to the active layer). A Fabry-Perot resonator is commonly used in the EELs, and it is formed with cleaved semiconductor facets/mirrors. Since light waves are tightly confined in the surface-normal direction more strongly than in the in-plane direction, the output beam tends to exhibit a highly asymmetric cross-section and a large beam divergence. In contrast, VCSELs generate light in a direction perpendicular to the active layer. In standard VCSELs, the active region, typically quantum wells, is fabricated between two distributed Bragg reflectors (DBRs), where the top reflector possesses a slightly lower reflectivity and serves as an output coupler. Comparing to EELs, VCSELs generate a less divergent symmetric beam. It is noteworthy that VCSELs are generally operated with multiple transverse modes. This is to achieve a high output power. However, the higher-order modes critically diminish the beam quality. To improve the beam quality, VCSELs should be operated in a single mode with a limited output power. To solve the VCSELs' drawback, photonic crystal surface-emitting laser (PCSELs), a new semiconductor laser that uses a photonic crystal integrated on top of the active layer (Fig. 1.3) has been developed [1.23–39]. The PCSELs exhibit single-mode spectra with a high output power.

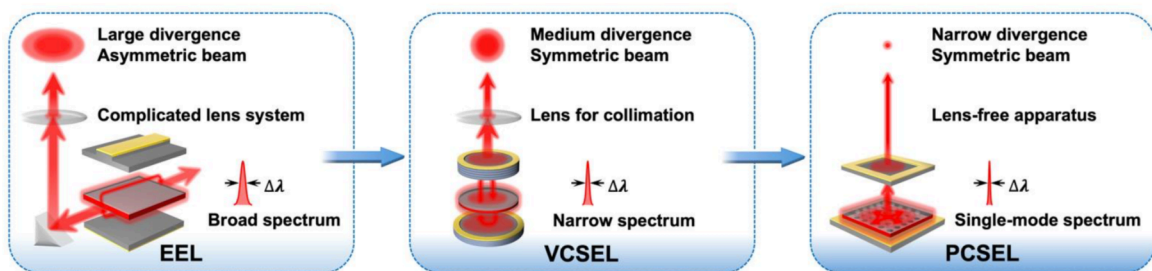


Figure 1.3. The schematic illustration in developing semiconductor lasers. Adopted from [1.39].

The standard VCSEL concept cannot be applied to QCL, since QCL has TM polarizations. Previous studies to achieve surface-emitting QCL used second-order Bragg gratings [1.40,41]. Alternatively, a few studies used two-dimensional PC slabs as a vertically emitting resonator [1.42–44].

1.1.3 Photonic crystals

A photonic crystal (PC) is an artificial medium, which has a periodic structure of refractive index. PC can be in one, two, or three dimensions [1.45–47]. The PCSEL commonly employs a two-dimensional PC. Figure 1.4 is a two-dimensional PC with a square-lattice structure. The important parameters building a two-dimensional PC include the refractive indices of periodic materials (n), the lattice constant (a), and the filling factor (ff). The unit cell is the smallest geometry, which cannot be reconstructed other than itself.

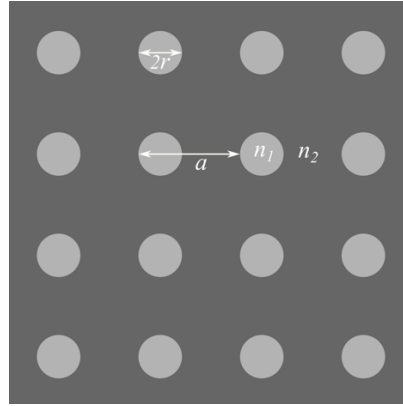


Figure 1.4. Square-lattice two-dimensional photonic crystal.

1.1.4 Photonic band structure

The periodic modulation of refractive index influences the properties of photons. The situation is similar with the properties of electrons in the periodic potential in semiconductors. Because of the periodicity, the permittivity is invariant under the primitive-lattice vector modulation.

$$\varepsilon(r + R) = \varepsilon(r) \quad (1.1)$$

where R refers to the primitive-lattice vector of the photonic crystals which is equal to $l_1 a_1 + l_2 a_2 + l_3 a_3$. In the periodicity of real space, the eigenvalues accomplish Bloch's theorem. Under the primitive-lattice modulation, the eigenvalues are invariant, contrary to the plane wave phase factor.

$$H(r) = e^{ik \cdot R} h_k(r) \text{ and } h_k(r + R) = h_k(r) \quad (1.2)$$

where k and h_k are the wave vector and the periodic function serves as a function of position in the Bloch function, respectively. The solution for wave propagation based on Maxwell's equations is as follows:

$$\nabla \times \left(\frac{1}{\varepsilon(r)} \nabla \times H(r) \right) = \frac{\omega^2}{c^2} H(r) \quad (1.3)$$

where $c = 1/\sqrt{\varepsilon_0\mu_0}$ is the speed of light in vacuum, and ω is the angular frequency. For the reciprocal space of periodic structure, the wave vector k also stays invariant under the reciprocal lattice modulation.

$$a_i \cdot b_j = 2\pi\delta_{ij} \quad (1.4)$$

where b_j is the reciprocal lattice vector, and δ_{ij} is the Kronecker symbol. The reciprocal space subjoins wave vector k with a particular eigenvalue and eigenfunction of the propagation wave. It can correspond to the band structure which shows the relationship of the angular frequency (ω) against wave vector (k). The region of the first Brillouin zone is restrained between $-\pi/a$ and π/a (Fig. 1.5(a)). For a one-dimensional homogenous medium which has a uniform permittivity or a non-dispersive material as shown in Fig 1.5(b), the solution of equation (1.3) is $\omega(k) = c/\sqrt{\varepsilon}$. The band is straight going up and then folding back at the band edge of the first Brillouin zone. Nevertheless, for a periodic structure with alternating permittivity, interference appears at the interface, and then generates a standing wave. Therefore, a band splitting (bandgap) is formed at the band edge of the first Brillouin zone as shown in Fig. 1.5(c) in which the first (red line) and second (blue line) bands refer to high-and low-permittivity region, respectively. The optical bandgap depends on the different permittivity of the periodic material and will be broader as a function of higher-permittivity contrast.

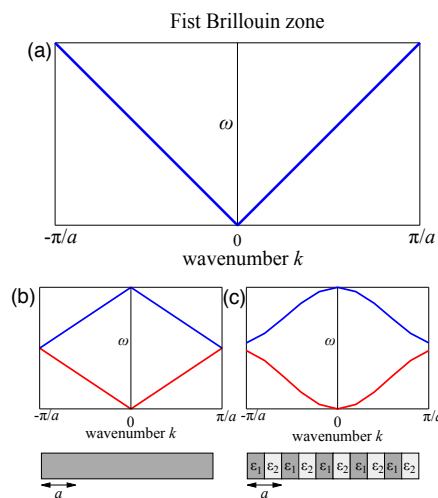


Figure 1.5. The band structure for a one-dimensional photonic crystal (a) the first Brillouin zone, (b) homogeneous material with uniform permittivity, and (c) periodic material with two different permittivity.

For a two-dimensional photonic crystal, the alternating periodicity of permittivity is displayed in two directions and is homogenous in one direction. For instance, Fig. 1.6 shows that the electromagnetic wave of light in a triangular photonic crystal propagates in the x - and y -directions and is homogenous in the z -direction. The electromagnetic field has two orthogonal polarizations, i.e., transverse electric (TE) and transverse magnetic (TM) modes. TE-polarization propagates the xy -plane electric field ($E_x, E_y, E_z = 0$) and out-of-plane magnetic field ($H_x = H_y = 0, H_z$). In contrast, TM-polarization is with the xy -plane magnetic field ($H_x, H_y, H_z = 0$) and out-of-plane electric field ($E_x = E_y = 0, E_z$). In particular structures, such as the hexagonal photonic crystal as shown in Fig. 1.6 (a), a real space is converted into a reciprocal space as illustrated in Fig 1.6 (b), which has high symmetry points at Γ, K , and M points in the first Brillouin zone [1.47].

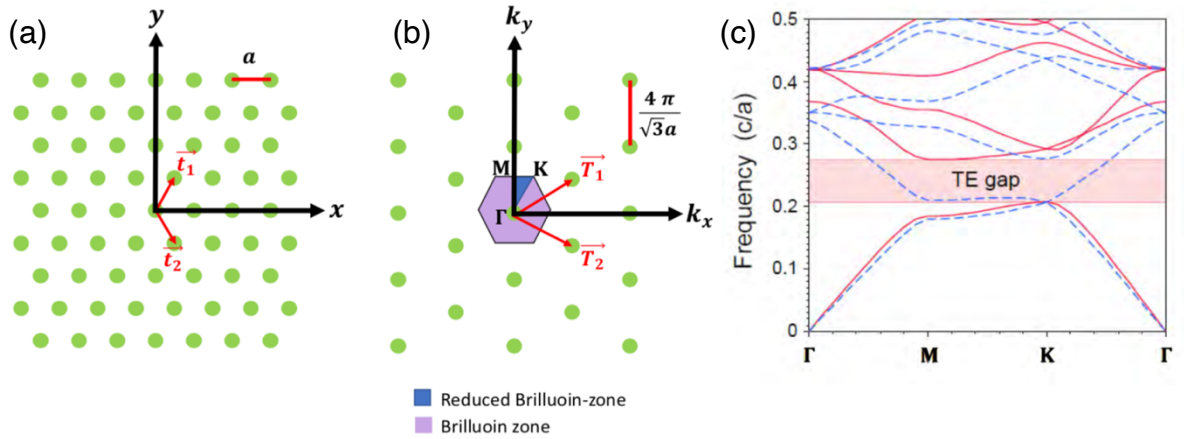


Figure 1.6. (a) Real space for a hexagonal photonic crystal. (b) Reciprocal space with high symmetry points Γ, K , and M points in the first Brillouin zone. (c) Photonic band structures. Images (a) and (b) are adopted from [1.48]. Image (c) is adopted from [1.46].

1.1.5 Quality factor

The quality factor (Q) of an optical resonator is a quantitative parameter that describes the resonator quality. The definition of Q is given by,

$$Q = 2\pi \frac{E_{\text{stored}}}{E_{\text{dissipated}}} \quad , \quad (1.5)$$

where E_{stored} is energy stored in the cavity and $E_{\text{dissipated}}$ is energy dissipated from the cavity per optical cycle. If the field energy decays with a decay rate constant Γ , i.e.,

$$\frac{d}{dt} E_{\text{stored}} = -\Gamma E_{\text{stored}} \quad ,$$

we have

$$E_{\text{dissipated}} = -\Delta E_{\text{store}} = \Gamma E_{\text{store}} \Delta t \quad , \quad (1.6)$$

where Δt is the optical cycle duration. Thus, the Q factor is written as

$$Q = \left(\frac{2\pi}{\Delta t} \right) \frac{1}{\Gamma} = \frac{\omega}{\Gamma} \quad , \quad (1.7)$$

where ω is the angular frequency at resonance. Since Γ^{-1} represents the lifetime of photons inside the cavity, the Q factor gives the effective cavity lifetime in the unit of ω^{-1} (optical cycle divided by 2π). Thus, a cavity with a higher Q factor has a longer lifetime and less dissipation. Hence, a higher Q leads to a lower lasing threshold.

In the following, we derive the Q factor for a typical edge-emitting semiconductor laser. We assume that the resonator consists of a material with refractive index n , and the Fabry-Perot cavity with length L has two identical mirrors with reflectance R . For simplicity, we assume no optical loss except mirror reflection. In this case, energy reduction per round trip is given by $(1-R) + R(1-R) = 1-R^2$. Since the round-trip time is given by $2nL/c$, where c is speed of light in vacuum, energy reduction per unit time, which is nothing but the definition of Γ , is given by

$$(1 - R^2) \frac{c}{2nL} = \Gamma \quad , \quad (1.8)$$

Thus, the Q factor in (1.7) is expressed as,

$$\begin{aligned} Q &= \frac{\omega}{\Gamma} = \frac{\omega}{1 - R^2} \frac{2nL}{c} \\ &= \frac{2\pi}{1 - R^2} \frac{2nL}{\lambda} \quad , \quad (1.9) \end{aligned}$$

where λ is optical wavelength in vacuum.

As a standard semiconductor laser, we adopt that $n = 3.5$, $R = 30\%$, $L = 1$ mm, and $\lambda = 640$ nm. Then, we have

$$\begin{aligned} Q &= \frac{2\pi}{(1 - 0.3^2)} \times \frac{2 \times 3.5 \times 1 \times 10^{-3} \text{ (m)}}{640 \times 10^{-9} \text{ (m)}} \\ &\approx 6.9 \times 10^5 \quad (1.10) \end{aligned}$$

Thus, the typical Q factor is expected to be on the order of $10^4 - 10^5$. It is noted that the expression of Q in Eq. 1.9 is inversely proportional to λ . Thus, the Q factor of QCL devices at midinfrared wavelengths could be an order of magnitude lower than the above value, which was determined for visible wavelength lasers.

1.2 Previous works

1.2.1 Progress in photonic crystal surface emitting lasers (PCSELs)

In PCSEL, the principle of laser action relies on the zero-group velocity of light at photonic band edges, which results in strong in-plane feedback inside the PC slab. Moreover, when the band edges are formed at the Γ point in momentum space, radiation into free space purely out of plane, i.e., normal to the slab.

PCSEL was first reported by M. Imada *et al.* in 1999 [1.23]. They demonstrated PCSEL by utilizing a semiconductor gain material and the Γ point of triangular-lattice photonic crystal. They successfully demonstrated coherent oscillation at the Γ point both in 1D and 2D photonic crystals [1.23,26]. Moreover, when the band edges are created at the Γ -point of the momentum space, radiation in free space occurs in the surface-normal (vertical) direction. At the same time, Meierl *et al.* demonstrated PCSELs by using organic gain materials and a triangular-lattice photonic crystal resonant at the band edge of the X or M point [1.24]. However, they obtained incoherent 2D oscillation because of the lack coupling inside 2D photonic crystal resonator at the band edge of the X or M point. The realizations of PCSELs which demonstrated stable and large-area coherent lasing at the Γ point were also reported by using a square-lattice photonic crystal [1.28,33]. Furthermore, the PCSELs have been investigated for a specific capability, such as to tailor of beam pattern and polarization [1.25,28], to emit tunable wavelengths [1.29,34], and to achieve both high-beam-quality and high-beam operation [1.32]. Recent views about current progress in PCSELs were reported by K. Ishizaki *et al.* and Y. H. Hong *et al.* in 2019 and 2022, respectively [1.37,39].

1.2.2 Surface emitting quantum cascade lasers

Surface emitting quantum cascade laser was first reported by R. Colombelli *et al.* in 2003 [1.42]. They applied a microcavity-resonator for QCLs (as shown in Fig. 1.9), which leads to vertical extraction of the laser light. By tuning the air hole radius or the lattice constant, they observed the resonance coupling between the PC and the gain spectrum. Later, surface emitting quantum cascade lasers in the mid- and far-infrared regions are reported by G. Xu *et al.* and Z. Wang *et al.* in 2010 and 2019, respectively [1.43,44].

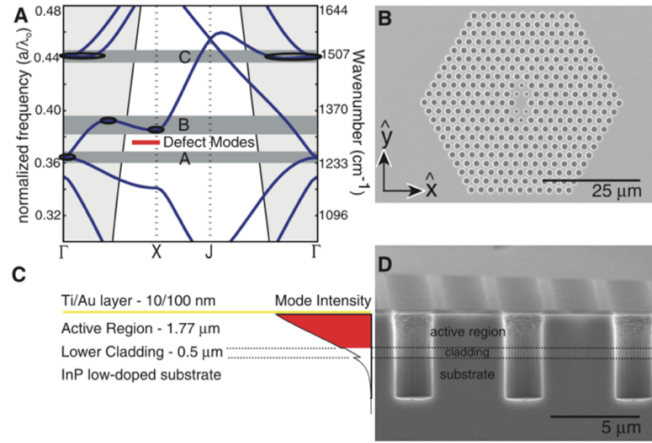


Figure 1.9. (a) Calculated TM-like band structure. Dark gray horizontal bands show the flat-band regions (A, B, and C). The thick red line shows the highly defect modes. (b) Top side view of scanning electron microscope (SEM). (c) The device structures and the intensity profile of surface plasmon mode. (d) Cross-sectional side view of SEM. Adopted from [1.42].

1.3 Remaining challenges

1.3.1 Characterization technique for photonic band structures in the midinfrared region

The angle-resolved observation of subthreshold luminescence spectra is a common technique to observe photonic band structures in visible- and near-infrared wavelength PCSELs. However, this technique cannot be applied to midinfrared wavelengths due to the limited sensitivity of infrared detectors. Moreover, the focused beam design in FT-IR makes it difficult to study angular dependent spectra. Therefore, a new technique to measure angle-resolved spectra is needed.

1.3.2 Photonic band structures in laser devices

In previous studies, PCSELs have been developed in the visible and near infrared region. To develop a midinfrared PCSEL, the in-plane dispersion relations of PC slabs with different pillar shapes and filling factors are required.

1.4 Outline of the thesis

This thesis consists of six chapters. Following the current chapter, in Chapter 2, I focus on developing a home-made optical setup for the angle-resolved reflection measurement. The optical setup is installed in the sample compartment of an FT-IR spectrometer. In standard FT-IR, the focused beam possesses an incident angle dispersion that exceeds 10° . Hence, we had

a difficulty for studying samples with angular dependence. To solve this problem, we propose a new technique to achieve a higher angle resolution.

In Chapter 3, I apply the angle-resolved measurement technique to the study of two-dimensional silicon-on-insulator (SOI) triangular-lattice PC slabs. We prepared samples with two different lattice constants, $a = 530$ and 560 nm. Due to their high refractive contrast, transverse electric (TE)-like and transverse magnetic (TM)-like modes are strongly split. We determine the PC band structures at the vicinity of the Γ point. By comparing the spectral width at normal incidence and that at the incident angle of 4° , we identify a peculiar optical phenomenon, namely Dirac cone materialized by effective degeneracy.

In Chapter 4, I measure reflection spectra and band structures in a square-lattice PC slab. The PC slab is formed of In(Ga, Al)As/InP-based multilayer structures and used as an actual PC-QCL device. We measure TM-like eigen modes at the vicinity of the Γ point. We find that each of the TE-like/TM-like mode consists of one doubly degenerate (E) and two nondegenerate modes. Due to the low refractive index contrast, TE-TM splitting is relatively small. We also make a spectral analysis to determine Q factors.

In Chapter 5, I focus on the impact of pillar shapes and filling factors on the resonator characteristics. We investigate and compare the resonance spectra of all the PC slabs around the Γ point. We also clarify the influence of filling factors on the intensity of reflection spectra.

In Chapter 6, I summarize these works and propose the future study.

References

- [1.1] J. Faist, F. Capasso, D. L. Sivco, C. Sirtori, A. L. Hutchinson, and A. Y. Cho, "Quantum cascade laser," *Science* **264**, 553 (1994).
- [1.2] J. Faist, *Quantum Cascade Lasers* (Oxford: Oxford University Press, 2013).
- [1.3] B. G. Lee, *Distributed Feedback Quantum Cascade Laser Arrays for Chemical Sensing* (PhD thesis, Harvard University, 2009).
- [1.4] R. D. Dupuis, P. D. Dapkus, N. Holonyak, E. A. Rezek, and R. Chin, "Room-temperature laser operation of quantum-well Ga(1-x)AlxAs-GaAs laser diodes grown by metalorganic chemical vapor deposition," *Appl. Phys. Lett.* **32**, 295 (1978).
- [1.5] R. D. Dupuis, P. D. Dapkus, N. Holonyak, and R. M. Kolbas, "Continuous room-temperature multiple-quantum-well AlxGa1-xAs-GaAs injection lasers grown by metalorganic chemical vapor deposition," *Appl. Phys. Lett.* **35**, 487 (1979).

- [1.6] R. Chin, N. Holonyak, B. A. Vojak, K. Hess, R. D. Dupuis, and P. D. Dapkus, “Temperature dependence of threshold current for quantum-well $\text{Al}_x\text{Ga}_{1-x}\text{As-GaAs}$ heterostructure laser diodes,” *Appl. Phys. Lett.* **36**, 19 (1980).
- [1.7] F. Capasso, “High-performance midinfrared quantum cascade lasers,” *Opt. Eng.* **49**, 111102 (2010).
- [1.8] Y. Yao, A. J. Hoffman, and C. F. Gmachl, “Mid-infrared quantum cascade laser,” *Nature Photon.* **6**, 432–439 (2012).
- [1.9] A. Bismuto, S. Blaser, R. Terazzi, T. Gresch, and A. Muller, “High performance, low dissipation quantum cascade lasers across the mid-IR range,” *Opt. Express* **23**, 5477–5484 (2015).
- [1.10] H. Yoshinaga, T. Kato, Y. Tsuji, H. Mori, J. Hashimoto, and Y. Iguchi, “Mid-infrared quantum cascade laser operable in high temperature (200 °C),” *SEI Technical Review* **90**, 94–98 (2020).
- [1.11] S. Saito, R. Hashimoto, K. Kaneko, T. Kakuno, Y. Yao, N. Ikeda, Y. Sugimoto, T. Mano, T. Kuroda, H. Tanimura, S. Takagi, and K. Sakoda, “Design and fabrication of photonic crystal resonators for single-mode and vertical surface emission from strain-compensated quantum cascade lasers operating at $4.32\ \mu\text{m}$,” *Appl. Phys. Express* **14**, 102003 (2021).
- [1.12] D. D. Nelson, J.H. Shorter, J. B. Mcmanus, and M.S. Zahniser, “Sub-part-per-billion detection of nitric oxide in air using a thermoelectrically cooled mid-infrared quantum cascade laser spectrometer,” *Appl. Phys. B* **75**, 343–350 (2002).
- [1.13] A. Kosterev, G. Wysocki, Y. Bakhirkin, S. So, R. Lewicki, M. Fraser, F. Tittel, and R. Curl, “Application of quantum cascade lasers to trace gas analysis,” *Appl. Phys. B* **90**, 165–176 (2008).
- [1.14] W. Ren, A. Farooq, D. F. Davidson, R.K. Hanson, “CO concentration and temperature sensor for combustion gases using quantum-cascade laser absorption near $4.7\ \mu\text{m}$,” *Appl. Phys. B* **107**, 849–860 (2012).
- [1.15] H. Yoshinaga, H. Mori, J. Hashimoto, Y. Tsuji, M. Murata, and T. Katsuyama, “Low power consumption (<1 W) mid-infrared quantum cascade laser for gas sensing,” *SEI Technical Review* **79**, 112–116 (2014).
- [1.16] Y. Bidaux, A. Bismuto, P. Patimisco, A. Sampaolo, T. Gresch, G. Strubi, S. Blaser, F. K. Tittel, V. Spagnolo, A. Muller, and J. Faist, “Mid infrared quantum cascade laser operating in pure amplitude modulation for background-free trace gas spectroscopy,” *Opt. Express* **24**, 26464–26471 (2016).

- [1.17] Y. Zhao, S. Tanaka, C.-C. Pan, K. Fujito, D. Feezell, J. S. Speck, S. P. DenBaars, and S. Nakamura, “High- power blue-violet semipolar (20-2-1) InGaN/GaN light-emitting diodes with low efficiency droop at 200 A/cm²,” *Appl. Phys. Express* **4**, 082104 (2011).
- [1.18] C.-C. Pan, S. Tanaka, F. Wu, Y. Zhao, J. S. Speck, S. Nakamura, S. P. DenBaars, and D. Feezell, “High-power, low-efficiency-droop semipolar (20-2-1) single-quantum-well blue light-emitting diodes,” *Appl. Phys. Express* **5**, 062103 (2012).
- [1.19] B. P. Yonkee, E. C. Young, C. Lee, J. T. Leonard, S. P. DenBaars, J. S. Speck, and S. nakamura, “Demonstration of a III-nitride edge-emitting laser diode utilizing a GaN tunnel junction contact,” *Opt. Express* **24**, 7816–7822 (2016).
- [1.20] F. Koyama, S. Kinoshita, and K. Iga, “Room-temperature continuous wave lasing characteristics of a GaAs vertical cavity surface-emitting laser,” *Appl. Phys. Lett.* **55**, 221 (1989).
- [1.21] C. J. Chang-Hasnain, M. Orenstein, A. Von Lehmen, L. T. Florez, J. P. Harbison, and N. G. Stoffel, “Transverse mode characteristics of vertical cavity surface-emitting lasers,” *Appl. Phys. Lett.* **57**, 218 (1990).
- [1.22] S. Stephan, D. Frederic, and A. Markus-Christian, “Novel InP- and GaSb-based light source for the near and far infrared,” *Semicond. Sci. Technol.* **31**, 113005 (2016).
- [1.23] M. Imada, S. Noda, A. Chutinan, and T. Tokuda, “Coherent two-dimensional lasing action in surface-emitting laser with triangular-lattice photonic crystal structure,” *Appl. Phys. Lett.* **75**, 316 (1999).
- [1.24] M. Meier, A. Mekis, A. Dodabalapur, A. Timko, R. E. Slusher, J. D. Joannopolous, and O. Nalamasu, “Laser action from two-dimensional distributed feedback in photonic crystals,” *Appl. Phys. Lett.* **74**, 7 (1999).
- [1.25] S. Noda, M. Yokohama, M. Imada, A. Chutinan, M. Mochizuki, “Polarization mode control of two-dimensional photonic crystal laser by unit cell structure design,” *Science* **293**, 1123–1125 (2001).
- [1.26] M. Imada, A. Chutinan, S. Noda, and M. Mochizuki, “Multidirectionally distributed feedback photonic crystal lasers,” *Phys. Rev. B* **65**, 195306 (2002).
- [1.27] K. Sakai, E. Miyai, T. Sakaguchi, D. Ohnishi, T. Okano and S. Noda, “lasing band-edge identification for a surface-emitting photonic crystal laser, *IEEE J. Sel. Areas Commun.* **23**, 1335–1340 (2005).
- [1.28] E. Miyai, K. Sakai, T. Okano, W. Kunishi, D. Ohnishi, and S. Noda, “Lasers producing tailored beam,” *Nature* **441**, 946 (2006).

- [1.29] H. Matsubara, S. Yoshimoto, H. Saito, Y. Jianglin, Y. Tanaka, and S. Noda, “GaN photonic-crystal surface-emitting laser at blue-violet wavelengths,” *Science* **319**, 445–447 (2008).
- [1.30] D. M. Williams, K. M. Groom, B. J. Stevans, D. T. Childs, R. J. E. Taylor, S. Khamas, R. A. Hogg, N. Ikeda and Y. Sugimoto, “Epitaxially regrown GaAs-based photonic crystal surface-emitting laser,” *IEEE Photonics Technol. Lett.* **24**, 966–968 (2012).
- [1.31] R. J. E. Taylor, D. M. Williams, J. R. Orchard, D. T. D. Childs, S. Khamas and R. A. Hogg, “Band structure and waveguide modelling of epitaxially regrown photonic crystal surface-emitting lasers,” *J. Phys. D: Appl. Phys.* **46**, 264005 (2013).
- [1.32] M. C. Soriano, J. Galcia-Ojalvo, C. R. Mirasso, and I. Fischer, “Complex photonics: Dynamics and applications of delay-coupled semiconductor lasers”, *Rev. Mod. Phys.* **85**, 421 (2013).
- [1.33] K. Hirose, Y. Liang, Y. Kurosak, A. Watanabe, T. Sugiyama, and S. Noda, “Watt-class high-power, high-beam quality photonic-crystal lasers”, *Nat. Photonics* **8**, 406-411(2014).
- [1.34] Z. L. Li, Y.C. Kang, G. Lin and C. P. Lee, “Mid-infrared photonic-crystal surface-emitting lasers with InGaAs/GaAsSb ‘W’-type quantum wells grown on InP substrate, *Photonics* **5**, 32 (2018).
- [1.35] H. Y. Lu, S. C. Tian, C. Z. Tong, L. J. Wang, J. M. Rong, C. Y. Liu, H. Wang, S. L. Shu, and L. J. Wang, “Extracting more light for vertical emission: high power continuous wave operation of 1.3- μm quantum-dot photonic crystal surface-emitting laser based on a flat band”, *Light: Science & Application* **8**, Article number: 108 (2019).
- [1.36] Y. Liang, Z. Wang, J. Wolf, E. Gini, M. Beck, B. Meng, J. Faist, and G. Scalari, “Room-temperature surface emission on large-area photonic crystal quantum cascade lasers”, *Appl. Phys. Letter* **114**, 031102 (2019).
- [1.37] K. Ishizaki, M. D. Zoysa, and S. Noda, “Progress in photonic-crystal surface-emitting lasers,” *Photonics* **6**, 96 (2019).
- [1.38] B. C. King, K. J. Rae, A. F. McKenzie, A. Boldin, D. Kim, N. D. Gerrard, G. Li, K. Nishi, K. Takemasa, M. Sugawara, R. J. E. Taylor, D. T. D. Childs, and R. A. Hogg, “Coherent power scaling in photonic crystal surface emitting laser arrays”, *AIP Advances* **11**, 015017 (2021).
- [1.39] Y. H. Hong, W. C. Miao, W. C. Hsu, K. B. Hong, C. L. Lin, C. Lin, S. C. Chen, and H. C. Kuo, “Progress of photonic-crystal surface emitting lasers: A Paradigm shift in LiDAR application,” *Crystal* **12**, 800 (2022).

- [1.40] D. Hofstetter, J. Faist, and M. Beck, “Surface-emitting 10.1 μm quantum-cascade distributed feedback lasers,” *Appl. Phys. Lett.* **75**, 3769 (1999).
- [1.41] W. Schrenk, N. Finger, S. Gianordoli, L. Hvozdar, G. Strasser, and E. Gornik, “Surface-emitting distributed feedback quantum-cascade lasers,” *Appl. Phys. Lett.* **77**, 2086 (2000).
- [1.42] R. Colombelli, K. Srinivasan, M. Troccoli, O. Painter, C. F. Gmachl, D. M. Tennant, A. M. Sergent, D. L. Sivco, A. Y. Cho, F. Capasso, “Quantum cascade surface-emitting photonic crystal laser,” *Science* **302**, 1374–1377 (2003).
- [1.43] G. Xu, R. Colombelli, R. Braive, G. Beaudoin, L. L. Gratiet, A. Talneau, L. Ferlazzo, and I. Sagnes, “Surface-emitting mid-infrared quantum cascade lasers with high-contrast photonic crystal resonators,” *Opt. Express* **18**, 11979–11989 (2010).
- [1.44] Z. Wang, Y. Liang, B. Meng, Y. T. Sun, G. Omanakutten, E. Gini, M. Beck, I. Sergachev, S. Lourdudoss, J. Faist, and G. Scarar, “Large area photonic crystal quantum cascade laser with 5 W surface-emitting power,” *Opt. Express* **27**, 22708–22716 (2019).
- [1.45] E. Istrate and E. H. Sargent, “Photonic crystal heterostructures and interfaces”, *Rev. Mod. Phys.* **78**, 455 (2006).
- [1.46] J. D. Joannopoulos, S. G. Johnson, J. N. Winn, and R. D. Meade, *Photonic Crystal: Molding the Flow of Light – Second edition* (Princeton University Press, 2008), rev – revised, 2 ed.
- [1.47] E. Armstrong, and C. O’Dwyer, “Artificial opal photonic crystals and inverse opal structures – fundamentals and applications from optics to energy storage”, *J. Mat. Chem.* **13**, 6019 (2015).
- [1.48] C. M. Patil, “Experiments on glide-symmetric photonic-crystal waveguides,” Ph.D. Thesis, University of Copenhagen, 2020.

Chapter 2 Method for high-precision angle-resolved measurement in the midinfrared region

2.1 Introduction

A common technique to study photonic band structures is the angle-resolved observation of subthreshold luminescence spectra. This technique has successfully been conducted in the visible and near-infrared region [2.1–3]. However, measurement of photonic band structures in the midinfrared region remains challenging. Therefore, we need to develop a new angle resolved technique, which is compatible with a Fourier-transform infrared (FTIR) spectrometer.

The FTIR spectrometer is a ubiquitous spectroscopic tool used in a wide range of material research [2.4,5]. Standard FTIR spectrometers have two optical configurations: transmission and reflection. Reflection measurement allows us to study optically thick and highly absorbing samples whose transmission spectra are difficult to obtain. Nevertheless, a rigorous Kramers-Kronig analysis of specular reflection spectra provides both the real and imaginary refractive indices of materials [2.6–8], the same information gained by transmission measurements of carefully prepared optically thin samples. Moreover, attenuated total reflection (ATR) techniques are used to measure the spectra of small amounts of samples [2.9–11]. The combination of an FTIR with Cassegrain-type objective lens or tip-enhanced near-field optic is capable of infrared imaging with a sub-micrometer resolution [2.12–14]. Such spatial resolution techniques, however, could fail to analyze the angular-dependent optical response inherent in anisotropic samples.

The loss of angular resolution is also a problem with standard FTIR architecture, where a thick beam from a Michelson interferometer is tightly focused on a sample. The angle of view at the sample position can reach $2\theta \sim 10^\circ$ (numerical aperture (NA) of ~ 0.17), which thus easily masks (or even eliminates) the angle-dependent fine resonance in infrared spectra. The optical design differs from that of ultraviolet-visible (UV-Vis) spectrometers, where a roughly collimated (unfocused) beam is transmitted through the sample. Thanks to the availability of large-area photodetector in the UV-Vis wavelength regions, a collimated beam passing through the sample compartment is directly coupled to the detector. In contrast, infrared detectors have much smaller apertures and thus require a focusing design for FTIR.

In this work, we develop angle-resolved midinfrared reflection setup with two design objectives. The first objective is to achieve a good collimation for the incident beam whose incident angle is tunable across zero, i.e., the normal incidence angle. The setup thus utilizes a

parabolic collimator or condensed pair, and infrared compatible beam splitter, which transmits the beam to the sample and reflects it to the detector. The beam shift associated with sample rotation is fully compensated for the setup. The second design objective is small footprint, which means that the setup can smoothly be installed in the sample compartment of a standard FTIR system. The modular design facilitates the flexibility of entire FTIR system in laboratories. As a demonstration of capability of the reflection setup, we measure angle-dependent midinfrared reflection spectra of two-dimensional photonic crystal (PC) slabs, which are fabricated on silicon-on-insulator (SOI) substrates [2.15].

2.2 Design and installation

We used FT/IR6800 (Jasco), which has a maximum resolution of 0.07 cm^{-1} , as a base FTIR spectrometer. It incorporates a liquid nitrogen cooled mercury cadmium telluride (MCT) detector, which has good sensitivity from 650 to $12,000\text{ cm}^{-1}$.

Figure 2.1 is an optical diagram of reflection setup. Infrared light from spectrometer is reflected by a flat steering mirror M1 to off-axial parabolic mirror PM1 that has a focal length of 25.4 mm (Thorlabs MPD019-M01). PM1 collimates the beam and sends it to another steering mirror M2. The beam is then directed to a 50:50 calcium fluoride beam splitter (BS; Thorlabs BSW510 for $\lambda = 2 - 8\ \mu\text{m}$). The beam transmitted through the BS as incident angle on a sample, which is mounted on a rotary stage. The sample reflects the beam and returns to the BS, which reflects it to a movable mirror M3. The motion of M3 fully compensates for the beam shift with changing the incident angle. When the sample is rotated by θ , M3 is rotated by $-\theta$, and translated along the optical axis so the beam follows the same path. Then, the beam passes through M4, PM2 (identical to PM1), and M5 to the instrument detector [2.16].

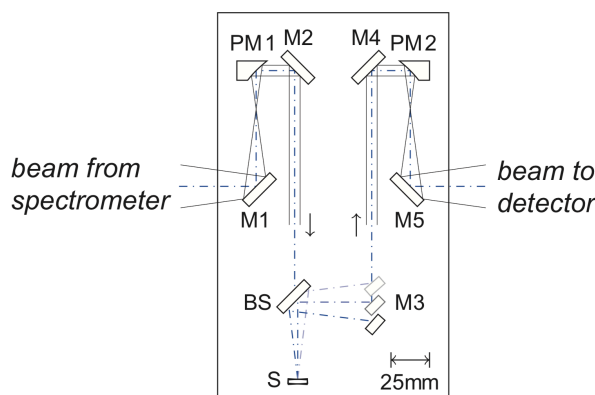


Figure 2.1. Optical diagram of the angle-resolved reflection setup. M1, M2, M4, and M5 plane mirror, PM1 parabolic collimator, BS beam splitter, S rotatable sample holder, M3 movable plane mirror, and

Pm2 parabolic condenser (Identical to PM1). The (blue) dash dotted line indicates the optical axis. All the optics are arranged on a 150 mm x 250 mm breadboard depicted by the rectangular frame [2.16].

An iris pair is inserted in between M2 and BS to reduce the beam diameter down to 1 mm, which is limited by the MCT sensitivity. All the optics are assembled on a 150 mm x 250 mm aluminum breadboard, which can be placed directly in the FTIR sample compartment (see the setup image in Fig. 2.2).

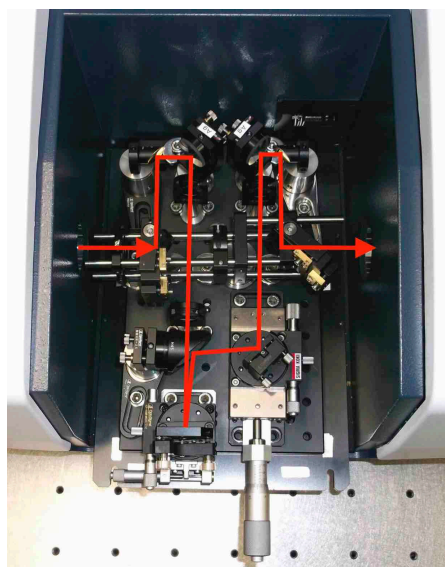


Figure 2.2. Photograph of the angle-resolved reflection setup, which is installed in FT/IR6800 (Jasco). The red line highlights the infrared beam path [2.16].

Proper optic alignment is essential to obtain a good angular resolution. The use of a visible light guide makes the alignment rather easy. In particular, we use a fiber coupled semiconductor laser as a point light source, and a fiber coupled photodiode as a small aperture detector. Before placing the optics, we carefully construct an alignment configuration with a visible light path (from source to detector), which imitated the infrared light path in FTIR. Note that we prepare this alignment configuration outside the FTIR system. We install the breadboard there and adjust all the optics position using visible light. After achieving a good condition, we move the breadboard (with all the optics in the correct place) to FTIR and carry out experiments. Note that the reflection setup reported in our earlier work utilized plan-concave lenses as a collimator or condensed pair [2.15]. Here, we replace the concave lenses with parabolic mirrors (PM1 and PM2) and remove chromatic aberration. Hence, optical

alignment using a visible laser, which has a wavelength far from IR light, is an efficient way to achieve optimal conditions.

2.3 Test performance

2.3.1 Estimation of angle resolution

Figure 2.3 shows the reflection intensity of a silver mirror mounted on the sample holder as a function of rotation angle. Here, we use the mirror as a reflection standard and define the intensity as the spectrally integrated intensity of FTIR output. The red circles show the intensity variation when the compensation optics (M3) does not move. The intensity peaks at zero, and then suddenly decreases when the mirror is rotated. Hence, the reflection setup is highly sensitive to the rotation (i.e., incident) angle. The full width half-maximum of the measured peak is evaluated to be 0.25° , which thus indicates the angle resolution of the setup. The blue diamonds show the intensity variation while we adequately move M3 to compensate for the beam shift associated with mirror rotation. The measured intensity remains almost constant even when the incident angle is changed, which ensures the stability of the setup. Currently, the tunable range of the incident angle is $\sim 8^\circ$, which is limited by the BS size (25.4 mm in diameter) and the M3 translator travel (25 mm). The tunable range could be extended by making minor changes.

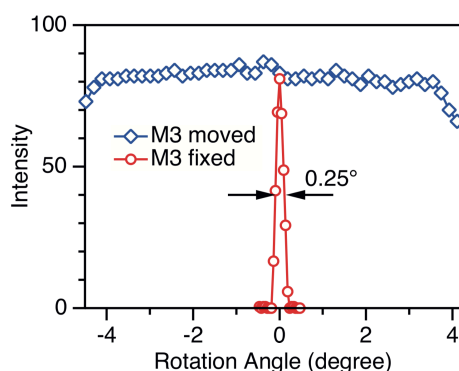


Figure 2.3. Mirror reflection intensity as a function of rotation angle. For the red circles, we rotate the-mirror holder, but we do not move the compensator (M3). For the blue diamonds, we move the compensator while simultaneously rotating the mirror [2.16].

The top panel in Fig. 2.4 shows the reflection spectrum of a bulk polymethyl methacrylate (PMMA) at normal incidence ($\theta = 0^\circ$). The spectrum indicates a variety of resonance peaks, which resembles the first derivative curves of symmetric absorption peaks assigned to different vibrational modes. The bottom panel shows the spectrum of the same PMMA measured using a commercially available variable-angle reflection accessory (Harrick Scientific, Seagull) at

near normal incidence ($\theta = 4^\circ$). The two spectra are almost identical thanks to the optical isotropy of PMMA. The homogenous sample exhibits a spectrum that is not very sensitive to the incident angles. Nevertheless, the measured spectral reproducibility ensures the accuracy of our hand-made setup.

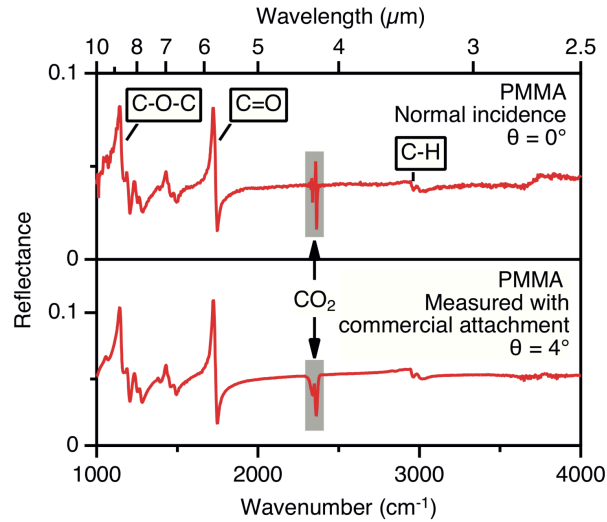


Figure 2.4. Reflection spectra of a bulk PMMA measured using our reflection setup normal incidence (top), and commercially available variable-angle reflection attachment, where the incident angle is set at 4° (bottom). Spectral noises associated with the absorption of CO_2 are indicated by the arrows. The assignments of several vibrational modes in PMMA are also indicated [2.16].

2.3.2 Midinfrared characterization of photonic crystal slabs

We apply the angle-resolved reflection setup to characterization of PC slab waveguides based on an SOI, which contains a top silicon layer with a thickness of 400 nm. The target PC design is a square lattice of air holes with a lattice constant of $2.27 \mu\text{m}$, a hole radius (R) of 526- nm, and a depth (d) of 216 nm. Figures 1.6 shows the photograph of seven PC slabs with different air-hole radii, ranging from 440 to 620 nm, and SEM images. The depth of air holes is 210 nm and the lattice constant is 2270 nm. The lateral area of each PC slab is 3 mm x 3 mm. These PC parameters lead to the formation of photonic Dirac cones, i.e., accidental degeneracy in the waveguide modes at the Γ point in the momentum space [2.17,18]. The samples are fabricated using a combination of electron beam lithography and reactive ion beam etching techniques. The design and fabrication are detailed elsewhere [2.15].

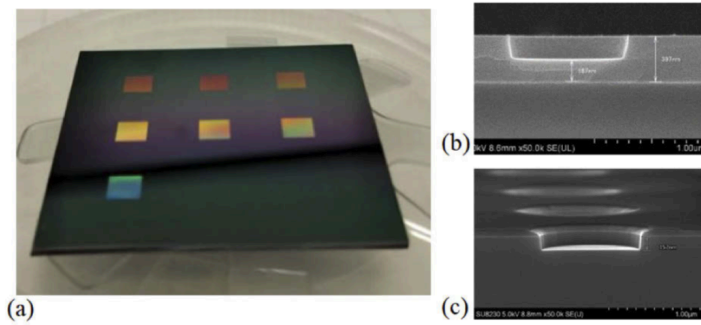


Figure 2.5. (a) Photograph of seven photonic crystal slabs with different air-hole radii fabricated in an SOI wafer. (b) and (c) SEM images of SOI square-lattice PC slab.

Figure 2.6 shows the normal incidence reflection spectrum of a PC sample together with that of an unprocessed SOI. Both spectra exhibit a slowly varying profile similar to a modulated sinusoid. Additionally, the PC sample spectrum has various small peaks. Thus, the slowly varying components appear due to Fabry–Perot interference occurring in the SOI, and the additional peaks arise due to resonant coupling between the incident light and the waveguide modes. Since the wavevector of light at normal incidence does not have a projection onto the slab layer, the incident light is only coupled to the waveguide mode at the Γ point ($k_{\parallel} = 0$). Consequently, the ensemble of sharp spectral lines represents the mode distribution at Γ as a function of frequency.

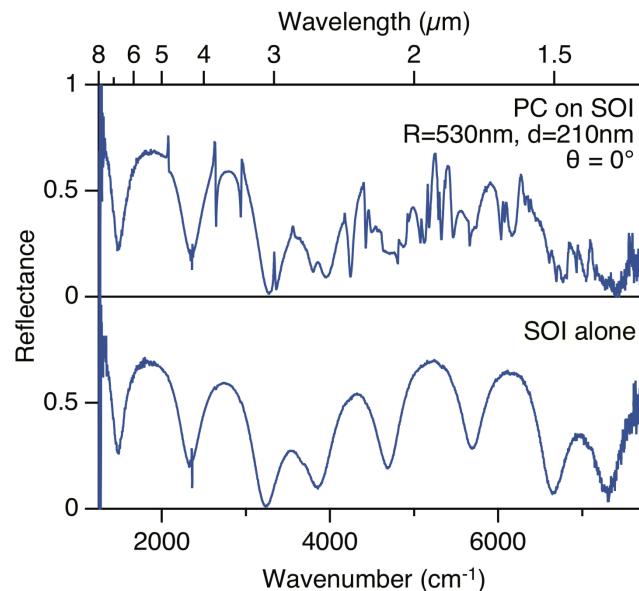


Figure 2.6. Midinfrared reflectance of an SOI PC slab ($R = 530 \text{ nm}$ and $d = 210 \text{ nm}$) at normal incidence. The spectrum of an unprocessed SOI is also shown at the bottom.

The top panel in Fig. 2.7(a) shows an expanded view of the normal incident spectrum at wavenumbers around $2,750\text{ cm}^{-1}$, i.e., the low frequency side of spectrum in Fig. 2.7. Four resonant peaks are found in this spectral range (highlighted by the vertical lines), and Dirac cones are expected to appear at the second lowest energy peak, as discussed later. The bottom panel in Fig. 2.7(a) shows the finite element calculation results, which perfectly reproduces the measured spectrum. Fig. 2.7(b) shows the spectra measured using common reflection accessories of FTIR: In the top panel, we use an infrared microscope with a Cassegrain optic with $\text{NA} = 0.45$ (x10 magnification, finite conjugate design), and in the bottom panel we use a standard variable angle reflection attachment (Harrick Scientific, Seagull). Neither spectrum exhibits clear resonance peaks, as they are masked due to the convolution of different spectra with distributed incident angles. The correct spectra are thus available for a sufficiently high angle resolution, which we have successfully achieved in this work.

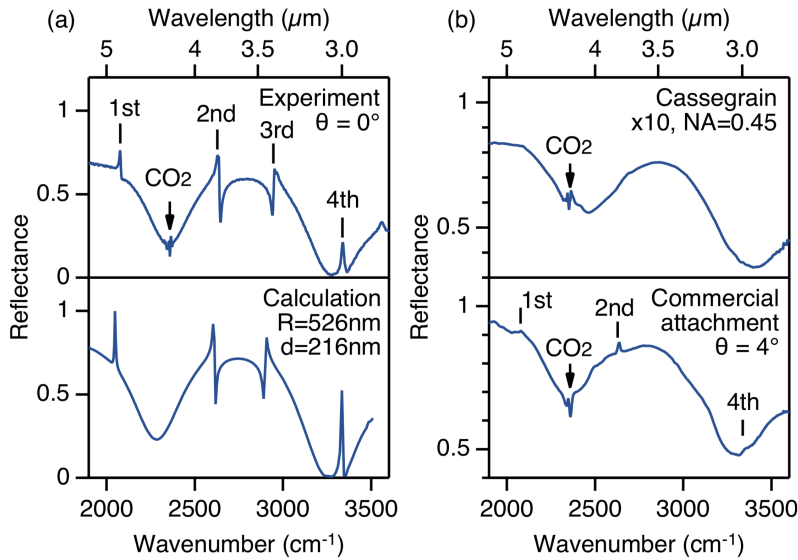


Figure 2.7. (a) Comparison of measured (top) and calculated (bottom) reflection spectra at normal incidence. We assume $R = 526\text{ nm}$ and $d = 216\text{ nm}$ for our calculation. Spectral noises associated with the absorption of CO_2 are indicated by the arrows. (b) Reflection spectra measured using a Cassegrain objective (top), and a commercial variable-angle reflection attachment, where the incident angle set to 4° (bottom) [2.16].

Figures 2.8(a) and 7(b) show the reflection spectra with different incident angles θ for samples with different hole radii. Here the incident beam is tilted in the incident plane toward the $[100]$ axis of the square PC lattice. Accordingly, the wavevectors is moved between Γ and X in the first Brillouin zone. The sample with $R = 530\text{ nm}$ (Fig. 2.7(a))

shows that the single peak at $\theta = 0^\circ$ splits into two peaks almost linearly with $|\theta|$. This is the signature of Dirac cones formed at Γ point. In contrast, the sample with $R = 440$ nm (Fig. 2.8(b)) exhibits a roughly parabolic energy shift in the vicinity of $\theta = 0^\circ$. In parallel, another new peak appears at finite θ values. The absence of the new peak at $\theta = 0^\circ$ reflects the optical selection rule of the PC mode [2.15]. Hence, no degeneracy is observed at $\theta = 0^\circ$ in this sample. Thus, we confirm the formation of Dirac cones in a sample that has a PC parameter close to the theoretically predicted value ($R = 526$ nm).

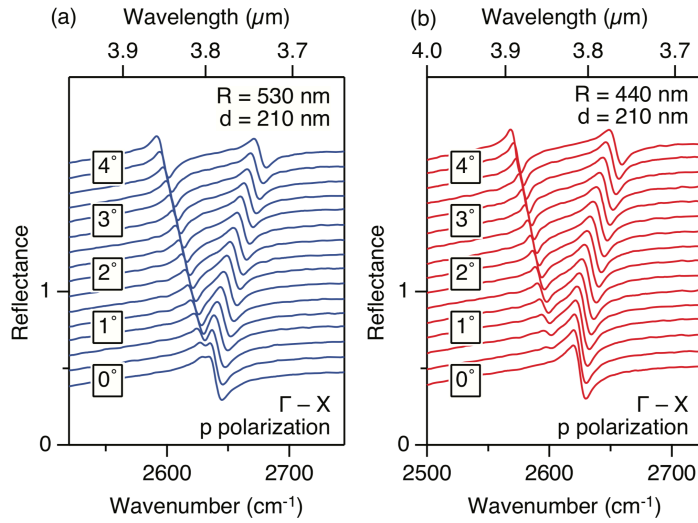


Figure 2.8. Incident angle dependent reflection spectra for PC slabs with (a) $R = 440$ nm. The spectra are arranged from bottom to top $\theta = 0^\circ$ to 4.38° in 0.292° steps. The incident beam is p-polarized and tilted towards the $[100]$ in-plane axis of the square-lattice sample [2.16].

2.4 Conclusion

We developed an angle-resolved reflection setup compatible with a standard FTIR spectrometer. The angle resolution reached 0.25° , which is not available with commercial products. The setup makes it possible to measure normal incidence spectra and to clarify the in-plane band dispersion of PC waveguides in the vicinity of the Γ point. Thus, one potential application of the setup is the study of PC surface-emitting lasers, which employ laser action at the Γ point. Photonic band characterization has already been realized by using angle-dependent sub-threshold luminescence measurement [2.19,20]. However, the technique cannot be applied to midinfrared lasers due to the limited sensitivity of infrared detectors. Our setup is expected to serve as a tool with which to clarify the in-plane waveguide dispersion and confirm vertical emission even in the midinfrared regions.

References

- [2.1] K. Sakai, E. Miyai, T. Sakaguchi, D. Ohnishi, T. Okano and S. Noda, “lasing band-edge identification for a surface-emitting photonic crystal laser, *IEEE J. Sel. Areas Commun.* **23**, 1335–1340 (2005).
- [2.2] D. M. Williams, K. M. Groom, B. J. Stevans, D. T. Childs, R. J. E. Taylor, S. Khamas, R. A. Hogg, N. Ikeda and Y. Sugimoto, “Epitaxially regrown GaAs-based photonic crystal surface-emitting laser,” *IEEE Photonics Technol. Lett.* **24**, 966–968 (2012).
- [2.3] R. J. E. Taylor, D. M. Williams, J. R. Orchard, D. T. D. Childs, S. Khamas and R. A. Hogg, “Band structure and waveguide modelling of epitaxially regrown photonic crystal surface-emitting lasers, *J. Phys. D: Appl. Phys.* **46**, 264005 (2013).
- [2.4] R. J. Bell, *Introductory Fourier Transform Spectroscopy* (Academic Press, 1972).
- [2.5] P. R. Griffiths and J. A. de Haseth, *Fourier Transform Infrared Spectrometry* (John Wiley and Sons, 2006).
- [2.6] B. Harbecke, “Application of Fourier’s allied integrals to the Kramers–Kronig transformation of reflectance data,” *Appl. Phys. A* **40**, 151–158 (1986).
- [2.7] K. Ohta and H. Ishida, “Comparison among several numerical integration method for Kramers–Kronig transformation,” *Appl. Spectrosc.* **42**, 952–957 (1988).
- [2.8] A. Kocak, S.L. Berets, V. Milosevic and M. Milosevic, “Using the Kramers–Kronig method to determine optical constants and evaluating its suitability as a linear transform for near-normal front-surface reflectance spectra,” *Appl. Spectrosc.* **60**, 1004–1007 (2006).
- [2.9] L. L. Lewis and A. J. Sommer, “Attenuated total internal reflection infrared mapping microspectroscopy of soft materials,” *Appl. Spectrosc.* **54**, 324–330 (2000).
- [2.10] B. M. Patterson and G. J. Havrilla, “Attenuated total internal reflection infrared microspectroscopic imaging using a linear array detector,” *Appl. Spectrosc.* **60**, 1256–1266 (2006).
- [2.11] G. van Dalen, P. C. M. Heussen, R. den Adel and R. B. J. Hoeve, “Attenuated total internal reflection infrared microscopy of multilayer plastic packaging foils,” *Appl. Spectrosc.* **61**, 593–602 (2007).
- [2.12] B. Knoll and F. Keilmann, “Near-field probing of vibrational absorption for chemical microscopy,” *Nature* **399**, 134–137 (1999).

- [2.13] T. Taubner, R. Hillenbrand and F. Keilmann, “Nanoscale polymer recognition by spectral signature in scattering infrared near-field microscopy,” *Appl. Phys. Lett.* **85**, 5064–5066 (2004).
- [2.14] R. Furstenberg, J. A. Soares and J. O. White, “Apparatus for the imaging of infrared photoluminescence, transmittance, and phototransmittance with high spatial and spectral resolution,” *Rev. Sci. Instrum.* **77**, 073101 (2006).
- [2.15] Y. Yao, N. Ikeda, T. Kuroda, T. Mano, H. Koyama, Y. Sugimoto and K. Sakoda, “Mid-IR Dirac-cone dispersion relation materialized in SOI photonic crystal slabs,” *Opt. Express* **28**, 4194–4203 (2020).
- [2.16] T. Kuroda, S. Chalimah, Y. Yao, N. Ikeda, Y. Sugimoto, and K. Sakoda, “Apparatus for high-precision angle-resolved reflection spectroscopy in mid-infrared region,” *Appl. Spectrosc.* **75**, 259–264 (2021).
- [2.17] K. Sakoda, “Dirac cone in two- and three-dimensional metamaterials,” *Opt. Express* **20**, 3898–3917 (2012).
- [2.18] K. Sakoda, “Proof of the universality of mode symmetries in creating photonic Dirac cones,” *Opt. Express* **20**, 25181–25194 (2012).
- [2.19] D. M. Williams, K. M. Groom, B. J. Stevens, D. T. D. Childs, R. J. E. Taylor, S. Khamas, R. A. Hogg, N. Ikeda and Y. Sugimoto, “Epitaxially regrown GaAs-based photonic crystal surface-emitting laser,” *IEEE Photonics Technol. Lett.* **24**, 966–968 (2012).
- [2.20] R. J. E. Taylor, D. M. Williams, D. T. D. Childs, B. J. Stevens, L. K. Shepherd, S. Khamas, K. M. Groom, R. A. Hogg, N. Ikeda and Y. Sugimoto, “All-semiconductor photonic crystal surface-emitting lasers based on epitaxial regrowth,” *IEEE J. Sel. Top. Quantum Electron.* **19**, 4900407 (2013).

Chapter 3 Symmetry assignment and formation of Dirac cones materialized by effective degeneracy

3.1 Introduction

The studies on photonic band structures have tremendously been conducted in recent years from novel points of view, the example of which include the observation of Dirac cone dispersion relation [3.1–3], cloaking by vanishing effective refractive index [3.4], and topological PCs and topological edges modes [3.5,6]. For these studies, a silicon-on-insulator (SOI) is used as a base waveguide because it possesses a high refractive index contrast.

In this chapter, we report angle-resolved reflection measurement results on triangular-lattice PC slabs fabricated in SOI. We obtain the dispersion relations and mode symmetry at the Γ point by analyzing the spectra. We also report the redistribution of diffraction loss between A_1 - and E_1 - symmetry modes, which originates from the Dirac-cone formation by *effective degeneracy*. A prior theoretical analysis about selection rules was reported by Y. Yao et al. [3.7].

3.2 Methods

3.2.1 Sample fabrication

PC slabs consisting of a triangular array of circular air holes were fabricated in a 400 nm-thick to Si layer of an SOI wafer (SOITEC) by electron beam (EB) lithography. Elionix ELS-7000 for EB exposure and Zenon ZEP520A as an EB resist were used. The top layer was etched by inductively coupled plasma reactive ion etching (ICP-RIE) with an etchant comprised of a mixture of Ar and Cl_2 . Five PC slabs with different design radii, r , of air holes, 500, 530, 560, 590, and 620 nm, we fabricated on the same SOI wafer, whose photograph is shown in Fig. 1(a). The lattice constant, a , and the air-hole depth, d , of the PC slabs were designed as 2400 and 240 nm, respectively. The top and side views of SEM image are shown in Figs. 3.1(b) and 3.1(c). The surface area of each PC was 3.4 mm ($= 1435 a$) by 3.5 mm ($= 1680 \sqrt{3}a/2$).

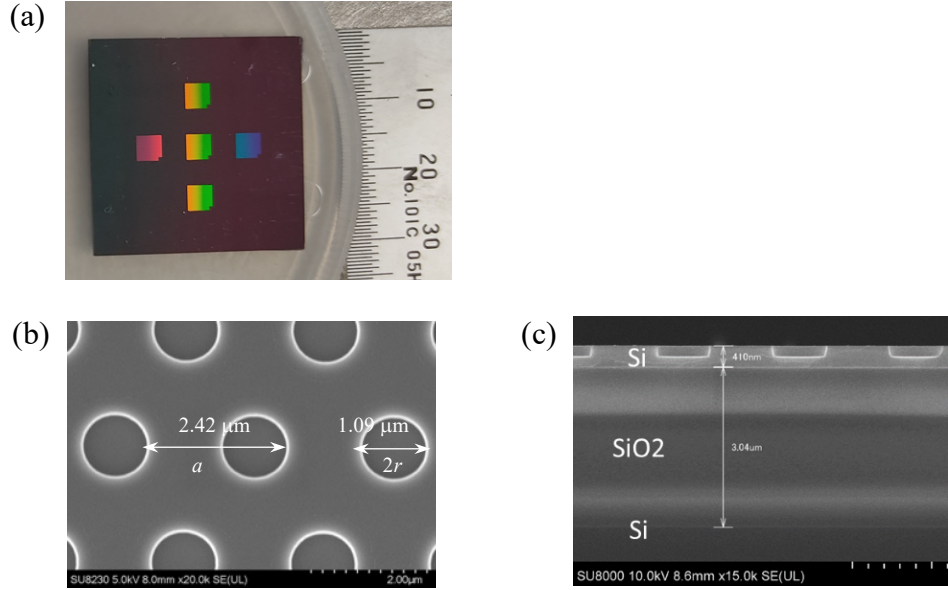


Figure 3.1. (a) Photograph of the five PCs fabricated in an SOI wafer. (b) Top and (c) cross-sectional side views of the SEM image of one of the five PCs with a design $r = 560$ nm. The top Si layer and the SiO_2 layer are 400 nm and 3 μm thick, respectively.

3.2.2 Angle-resolved reflection measurement

Angle-resolved reflection spectra were measured by using our home-made high-resolution setup, which was placed in the sample chamber of a Fourier transform infrared (FTIR) spectrometer (JASCO 6800) with a high-intensity ceramic light source as explained above in Chapter 2 [3.8]. The measurement configuration is illustrated in Fig. 3.2, where the first Brillouin zone of the triangular lattice and its highly symmetric point (Γ , K, and M points) are shown as an inset. The tilt angle from the normal (z) direction and the azimuthal angle from the x axis are denoted by θ and ϕ , respectively.

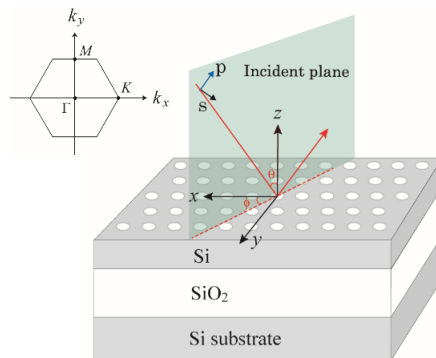


Figure 3.2. Configuration of the incident plane wave. The tilt angle from the normal (z) direction and the azimuthal angle from the x axis are denoted by θ and ϕ , respectively. The polarization of the incident wave is denoted by p (s) when its electric field is parallel (perpendicular) to the incident plane. The inset shows the first Brillouin zone of the 2D triangular lattice.

3.2.3 Theory

The dispersion relation and the angle-resolved reflection spectra were calculated by the finite element method (FEM) with the commercial software, COMSOL. The Bloch boundary condition was imposed on the unit cell in the lateral (x and y) directions. The perfectly matched layer (PML) absorbing boundary condition was imposed in the vertical (z) direction. The results of the calculation will be presented in Section 3.

The selection rules for reflection peaks are summarized in Table 3.1, which was obtained for six irreducible representations of the C_{6v} point group. They represent the symmetries of eigen modes on the Γ point [3.9]. Not that the electric field is a genuine vector and the magnetic field is an axial vector, so their symmetry properties are generally different. Table 3.1 is referred to the symmetry of the magnetic field. E_1 - and E_2 -symmetric modes are doubly generate and the other four modes are nondegenerate. Among these irreducible representations, only E_1 -symmetric modes are active to the incident plane wave from the normal (z) direction because this incident wave conserves the lateral component of the wave vector when it excites the eigenmodes on the Γ point and its symmetry-matched only to the E_1 -symmetric modes [3.9].

Modes on the Γ point connect to those on adjacent points in the first Brillouin zone according to the compatibility relations [3.9], so the symmetry of the latter by a purely analytical manner. In the $\Gamma - K$ and $\Gamma - M$ directions, all eigenmodes are symmetric or antisymmetric about the incident plane. So, when polarized incident whose the electric field is parallel (p) or perpendicular (s) to the incident plane is used, there are additional selection rules as listed in Table 3.1.

Table 3.1. Selection rules for reflection peaks

Mode symmetry	Γ ($\theta = 0^\circ$)	Γ -K direction ($\phi = 0^\circ$)	Γ -M direction ($\phi = 90^\circ$)
A_1	inactive	s	s
A_2	inactive	p	p
B_1	inactive	s	p
B_2	inactive	p	s
E_1	active	s, p	s, p
E_2	inactive	s, p	s, p

In addition, the symmetry and the number of eigenmodes on the Γ point by using a group theoretical analysis based on the zone-folding of dispersion curves of planar wave guides

without periodic modulation of the refractive indices, which relies on the *reduction* of reducible representation given by the superposition of the planar waveguide modes was explained [3.9]. In the present case, as it will be discussed in Section 3, the relevant eigenmodes mainly originate from the transverse electric (TE) modes of the SOI wafer and the reciprocal lattice vector for the zone-folding is the second smallest one. In this case, it can be proven by reduction procedure that there are E_{1-} , E_{2-} , A_{1-} , and B_{1-} symmetric modes [3.9]. An exception is the emerge of an A_{2-} -symmetric mode which originates from the zone-folding of a transverse magnetic (TM) waveguide mode by the smallest reciprocal lattice vector.

3.3 Results and discussions

3.3.1 Angle-resolved reflection spectra

For all PC specimens, there are three peaks for normal incidence ($\theta = 0^\circ$) in the spectral range 2,000 to 3,500 cm^{-1} , which are attributed to E_{1-} -symmetric eigenmodes according to the selection rules for the Γ point (see Table 3.1). From this observation, the conclusion is that there are three groups of eigenmodes that have different origin. By comparing their frequencies with those of waveguide modes of the SOI wafer, the first peak around 2,300 cm^{-1} and the second peak around 3,150 cm^{-1} , originated from the lowest TE and TM bands, respectively, which were folded into the first Brillouin zone with the smallest reciprocal lattice vector, whereas the third peak around 3,280 cm^{-1} originated from the lowest TE band, which was folded into the first Brillouin zone with the second smallest reciprocal lattice vector were found.

In the following, the discussion will be focused on the third group and present detailed analyses of reflection spectra for $r = 530$ and 560 nm. First, Fig. 3.3 shows the reflection spectra for $r = 530$ nm, where the azimuthal angle of the incident light was chosen to excite eigenmodes along Γ -K ($\phi = 0^\circ$) and Γ -M ($\phi = 90^\circ$) directions. For each azimuthal angle, the reflection spectra were measured with s- and p-polarized incident waves. In each panel of Fig. 3.3, nine spectra measured from $\theta = 0^\circ$ to 4° are presented, where adjacent spectra are shifted vertically by 0.5.

As aforementioned, there is a peak at 3,280 cm^{-1} originating from an E_{1-} -symmetric eigenmode for $\theta = 0^\circ$. When the tilt angle is increased, this peak shift and several new peaks appear. Their peak frequencies are plotted as functions of the lateral component of the wave vector of the incident light in Fig. 3.4(a), where the horizontal axis denotes the wave vector in the Γ -K and Γ -M directions, and M/10 and K/10 imply that the horizontal axis is magnified by ten times. s- and p- active peaks are marked by red and blue colors, respectively. Note that the

third and fourth highest bands are nearly degenerate at 3,280 cm^{-1} , although their peaks disappear on the Γ point. Also note that their two bands are active to s- and p-polarizations for each direction. These features agree with the properties of the E_2 -symmetric mode (see Table 3.1).

There are three more bands in Fig. 3.4(a), two of which should be attributed to A_1 - and B_1 -symmetric mode as aforementioned in Section 3.3.3, which are accompanied by two s-active bands in the Γ -K direction and by an s-active band and a p-active band in the Γ -M direction according to the Table 3.1. Then, the remaining band is a p-active band in each direction. By consulting Table 3.1 again, the conclusion is that the remaining bands should connect to A_2 -symmetric mode on the Γ point. The peak position of this A_2 -symmetric mode, or its eigenfrequency, strongly depends on the air-hole radius, r . When r is decreased, its eigenfrequency decreases and moves away from the frequencies of the third group. So, the conclusion can be that the A_2 -symmetric mode belongs to the second group, which originated from the lowest TM band of the SOI wafer.

The dispersion relation was calculated by FEM. By comparing the observed and calculated eigen frequencies of E_1 -symmetric modes, there is a discrepancy of about 40 cm^{-1} between them, which should be attributed to calculation and fabrication errors, ambiguity in the refractive indices, and ambiguity in the structural of the SOI wafer. The calculation owns a good agreement with the observation when the value for the air-hole depth, d , is assumed to be larger by 20%, which is 288- nm. Fig. 3.4(b) shows the dispersion relations thus calculated for $r = 530 \text{ nm}$, where the symmetry of eigen modes on the Γ point was obtained by examining their field distributions by the FEM calculations. Both dispersion curves and symmetry assignment agree well between the observations and calculations.

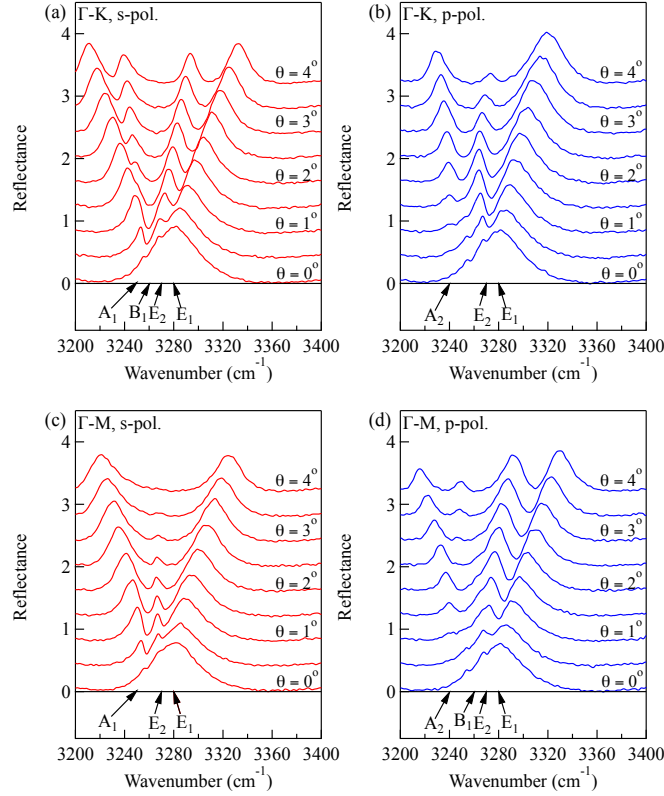


Figure 3.3. Angle-resolved reflection spectra of the specimen with $r = 530$ nm. Red (blue) lines denote spectra measured with an s- (p-) polarized incident wave. Arrows on the bottom of each panel show approximated locations of eigenmode frequencies on the Γ point, which are obtained by interpolating the peak frequency as a function of the lateral component of the incident wave vector in Fig. 3.4(a).

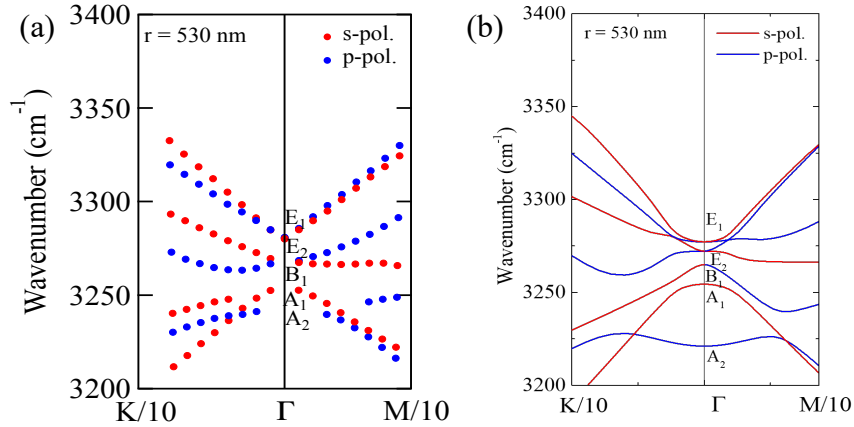


Figure 3.4. Dispersion $r = 530$ nm obtained (a) from Fig. 3.3 and (b) by numerical calculations. The horizontal axis is the wave vector in the first Brillouin zone. Red (blue) color denotes s- (-)p active bands. Refractive indices were assumed to be 3.427 for Si [3.10] and 1.440 for SiO₂ [3.11].

Next, Figure 3.5 shows the reflection spectra for $r = 560$ nm. Their features to obtain the dispersion relation and assign the mode symmetry as shown in Fig. 3.6(a) were analyzed as

before. Because the averaged refractive index was decreased by increasing the air-hole radius, the eigen frequencies generally increased, which is apparent when they are compared on the Γ point with those in Fig. 3.4(a). In addition, it is observed that the order of the modes on the Γ point have changed, which was caused by the difference in the radius of their eigen frequency. These features are well reproduced by numerical calculation as shown in Fig. 3.6(b).

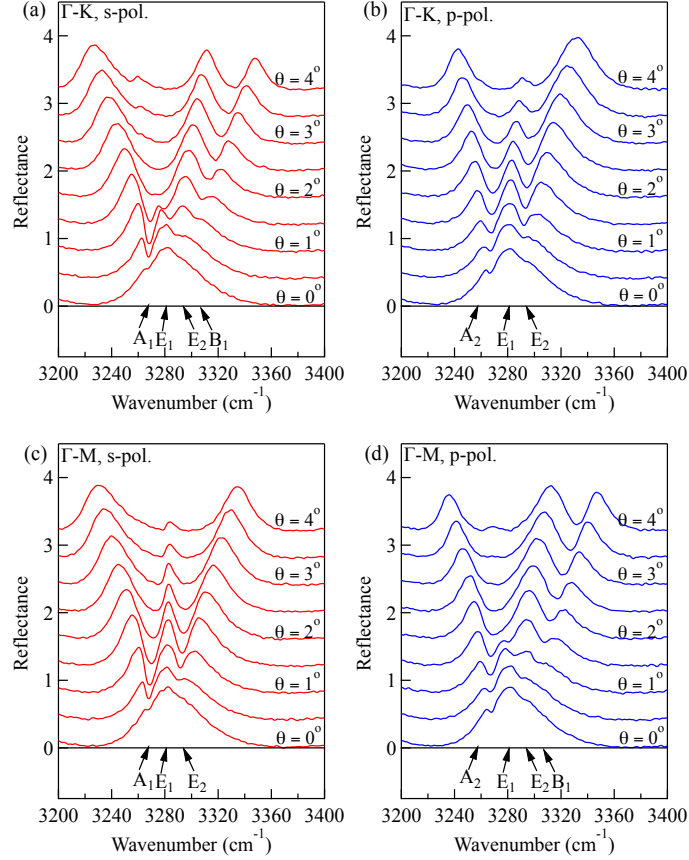


Figure 3.5. Angle-resolved reflection spectra of the specimen with $r = 560$ nm. Red (blue) lines denote spectra measured with an s- (p-) polarized incident wave. Arrows on the bottom of each panel show approximated locations of eigenmode frequencies on the Γ point, which are obtained by interpolating the peak frequency as a function of the lateral component of the incident wave vector in Fig. 3.6(a).

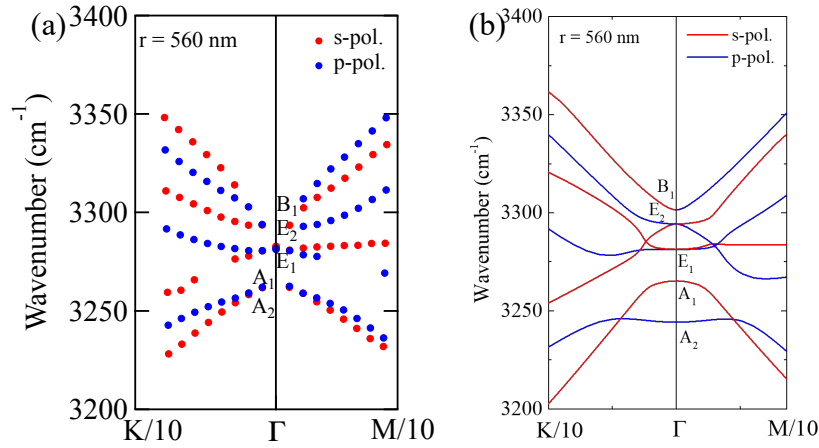


Figure 3.6. Dispersion $r = 560$ nm obtained (a) from Fig. 3.5 and (b) by numerical calculations. The horizontal axis is the wave vector in the first Brillouin zone. Red (blue) color denotes s- (-p) active bands.

Figure 3.7 is the reflection spectra calculated by FEM. It is assumed that $r = 560$ nm and $d = 240$ nm for this calculation. Not only the peak positions but also their spectral intensities are well reproduced, which further support the validity of these analyses.

In the recent publication [3.7], it is shown that by the method of $\mathbf{k}\cdot\mathbf{p}$ perturbation that a distorted Dirac cone was materialized by the accidental degeneracy of an E_1 -symmetric mode and an A_1 -/ A_2 -symmetric mode. Originally, the Dirac cone is characterized by a linear dispersion in the vicinity of the Γ point [3.1–3]. However, if the quality factor of the E_1 -symmetric mode is small due to a large diffraction loss, the deviation from the linear relation becomes apparent and their dispersion is characterized by an *exceptional point* [3.12,13]. In addition, the mixture of the E_1 -symmetric mode with the A_1 -/ A_2 -symmetric mode results in the redistribution of the diffraction loss. As a consequence, the two peaks of the Dirac cone have the same width, which is one half of the original width of the E_1 -symmetric mode [3.7].

For the present specimen, exact accidental degeneracy with the E_1 -symmetric mode was not observed. However, the spectral width of the E_1 -symmetric mode of the third group was larger (FWHM = 54.6 cm^{-1}), so A_1 - and A_2 -symmetric eigen modes whose eigen frequencies are located in the range can be regarded as effectively degenerate. This situation is materialized for the A_1 - and E_1 -symmetric modes in Figs. 3.6(a) and 3.6(b). Although there is also an A_2 -symmetric mode in the vicinity of the E_1 -symmetric mode, the former, which is a TM-like mode, has a character from the latter, which is a TE-like mode, so their mixing is generally small and we can safely neglect it when the discussion is about the mode mixing. For example,

the lowest peaks in Figs. 3.5(c) and 3.7(c), which has the A_1 -origin, has considerably large width due to the mixing with the E_1 -symmetric mode. Its width measured at $\theta = 4^\circ$ ($= 31.4 \text{ cm}^{-1}$) is approximately one half of the width of the E_1 -symmetric mode on the Γ point ($= 54.6 \text{ cm}^{-1}$). This feature was also confirmed by numerical calculation. The Q factor of the A_1 -origin mode at $\theta = 4^\circ$ was 123 whereas that of with the E_1 -symmetric mode was 61. So, the spectral width of the former should be one half of the latter, which agrees well with the theoretical results of Ref. [3.7].

On the other hand, the experimental observation of the Dirac cone dispersion relation was difficult for the present specimens of the triangular-lattice PCs because the photonic bands were densely present and their spectra overlapped each other. The observation of accidental degeneracy of E_1 - and E_2 -symmetric modes, which materializes double Dirac cone [3.3], was particularly difficult. A PC slab specimen that materializes a somewhat isolated E_1 - E_2 mode pair for this purpose. Its fabrication remains as a future challenge. When it is materialized, the effective refractive index at Dirac point is equal to zero, so we can expect peculiar phenomena like cloaking and propagation through sharply bent waveguides [3.1,4].

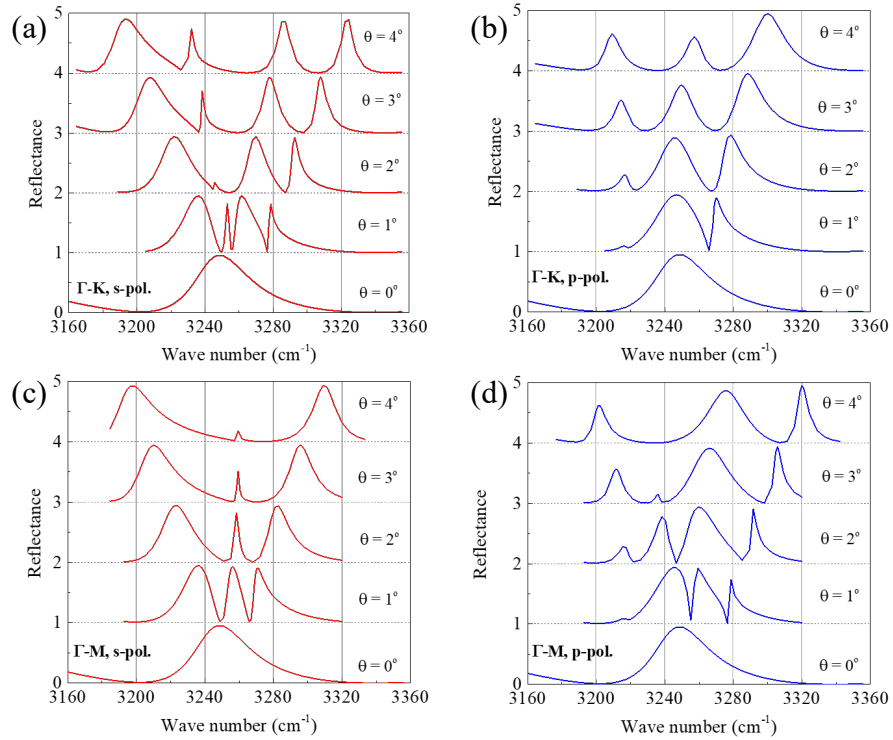


Figure 3.7. Angle-resolved reflection spectra for $r = 560$ and $d = 240$ nm calculated by FEM.

3.4 Conclusion

We presented the accurate measurements of angle-resolved spectra of triangular-lattice PC slabs fabricated in a standard SOI wafer by our home-made high-resolution setup integrated inside of an FTIR spectrometer. Their dispersion relation and mode symmetries by combining the observed peak positions and the selection rules expected for the C_{6v} -symmetric structure were demonstrated. Thus, the selection rules are a powerful tool to distinguish PC bands of different symmetry origin were proven. Although accidental degeneracy of modes was not observed in the present specimens, an effective degeneracy of an E_1 -symmetric mode and an A_1 -symmetric mode was materialized, which resulted in the redistribution of the diffraction loss from the former to the latter. The feature was confirmed by observed spectral widths and calculated Q factors.

References

- [3.1] X. Huang, Y. Lai, Z. H. Hang, H. Zheng, and C. T. Chan, “Dirac cones induced by accidental degeneracy in photonic crystal and zero-refractive index materials,” *Nat. Mater.* **10**, 582–586 (2011).
- [3.2] J. Mei, Y. Wu, C. T. Chan, and Z. -Q. Zhang, “First-principles study of Dirac and Dirac-like cones in phononic and photonic crystals,” *Phys. Rev. B* **86**, 035141 (2012).
- [3.3] K. Sakoda, “Proof of the universality of mode symmetries in creating photonic Dirac cones,” *Opt. Express* **20**, 25181–25194 (2012).
- [3.4] I. V. A. K. Reddy, V. Sukhotskiy, A. Baev, K. Liu, J. W. Haus, K. Sakoda, E. Furlani, J. Liu, S. Wen, and P. N. Prasad, “Quasi-triply-degenerate states and zero refractive index in two-dimensional all-dielectric photonic crystals,” *Opt. Express* **28**, 5548–5554 (2020).
- [3.5] L.-H. Wu and X. Hu, “Scheme for achieving a topological photonic crystal by using dielectric materials,” *Phys. Rev. Lett.* **114**, 223901 (2015).
- [3.6] S. Barik, A. Kurasahin, C. Flower, T. Cai, H. Miyake, W. DeGottardi, M. Hafezi, and E. Waks, “Quasi-triply-degenerate states and zero refractive index in two-dimensional all-dielectric photonic crystals,” *Science* **359**, 666–668 (2018).
- [3.7] Y. Yao, T. Kuroda, N. Ikeda, T. Mano, H. Koyama, Y. Sugimoto, and K. Sakoda, “Angle-resolved reflection spectra of Dirac cones in triangular-lattice photonic crystal slabs,” *Opt. Express* **28**, 21601–21615 (2020).

- [3.8] T. Kuroda, S. Chalimah, Y. Yao, N. Ikeda, Y. Sugimoto, and K. Sakoda, “Apparatus for high-precision angle-resolved reflection spectroscopy in mid-infrared region,” *Appl. Spectrosc.* **75**, 259–264 (2021).
- [3.9] K. Sakoda, *Optical Properties of Photonic Crystals* (Springer, 2004), 2nd edn.
- [3.10] D. Chandler-Horowitz and P. M. Amirtharaj, “High-accuracy, midinfrared refractive index values of silicon,” *J. Appl. Phys.* **97**, 123526 (2005).
- [3.11] I. H. Malitson, “Interspecimen comparison of the refractive index of fused silica,” *J. Opt. Soc. Am.* **55**, 1205–1209 (1965).
- [3.12] K. Sakoda and H. Takeda, “Dirac cones in photonic crystal slabs,” in *Program and Abstract Book of 10th International Symposium on Modern Optics and its Applications* (2015), pp. 68–69
- [3.13] B. Zhen, C. W. Hsu, Y. Igarashi, L. Lu, I. Kaminer, A. Pick, S.-L. Chua, J. D. Joannopoulos, and M. Soljacic, “Spawning rings of exceptional points out of Dirac cones,” *Nature* **525**(7569), 354–358 (2015).

Chapter 4 C_{4v} -symmetry photonic crystal slabs for application to photonic crystal surface-emitting quantum-cascade lasers

4.1 Introduction

As aforementioned, PCSELS exploit laser action at photonic band edges. Hence, careful PC design that realizes perfect resonance between the band-edge mode and the material gain frequencies is essential for the operation. The measurement of in-plane dispersion relations is thus required to verify optimum conditions of fabricated devices.

Here, we apply our angle-resolved reflection technique [4.1] to the characterization of actual PCSEL devices, which are formed by In(Ga,Al)As/InP-based QCL multilayer structures. The complex PC modes in the vicinity of the Γ point are identified with the aid of rigorous polarization-selection rules derived by group theory [4.2]. Moreover, spectral analysis makes it possible to evaluate the Q factors of the waveguide modes semi-quantitatively.

4.2 Methods

4.2.1 Samples

Midinfrared QCL multilayer structures are grown on n^+ InP (100) by molecular-beam epitaxy. We grow a lattice-matched (In, Ga)As buffer layer with a thickness of $1.0 \mu\text{m}$, an InP bottom cladding layer with a thickness of $2.5 \mu\text{m}$, and a thin (In, Ga)As guiding layer with a thickness of $0.3 \mu\text{m}$, followed by (In, Ga)As/(In, Al)As strain-compensated multiple quantum wells (MQWs) with a total thickness of $1.6 \mu\text{m}$. We then grow a $1.0\text{-}\mu\text{m}$ -thick (In, Ga)As layer, which we use for PC processing (for the layer sequence and expected refractive indices, see Fig. 4.1(a)).

Three-millimeter-square PC slabs with $a = 1.33, 1.36, \text{ and } 1.39 \mu\text{m}$ are fabricated using electron-beam lithography and reactive ion-beam etching techniques. (SiO_2 is used as a mask for the dry etching.) Note that the final PCSEL devices have another InP layer on top, which serves as a top cladding layer and then (In,Ga)As pillars are embedded, followed by a metal gate. This research study samples before InP regrowth and metal-gate deposition. The laser action of the final PCSEL devices was reported in Ref. [4.3].

4.2.2 Angle-resolved reflection measurement

Midinfrared angle-resolved reflection measurements are performed using a Fourier transform spectrometer (Jasco, FT/IR-6800) attached to a home-built variable-angle apparatus, where infrared light is carefully collimated and beam divergence is limited to less than 0.3° .

The collimated beam passes through an infrared beam splitter, which then transmits the beam from the sample to the detector. The setup enables to observe reflection spectra even at normal incidence and to change the incident angle (θ) from -3.7° to $+3.7^\circ$ across zero. A wire-grid polarizer is inserted into the beam path and it allows us to resolve the p- and s-polarized components, which have the electric field parallel and perpendicular to the incident plane, respectively. The design, which is detailed in Ref. [4.1] /Chapter 2, makes it possible to determine the mode frequencies as a function of in-plane wave vector and dispersion relation in the vicinity of the Γ point.

The measurement configuration is illustrated in Fig. 4.1, where the first Brillouin zone of the square lattice and its highly symmetric point (Γ , X, and M points) are shown as an inset. The tilt angle from the normal (z) direction and the azimuthal angle from the x axis are denoted by θ and ϕ , respectively.

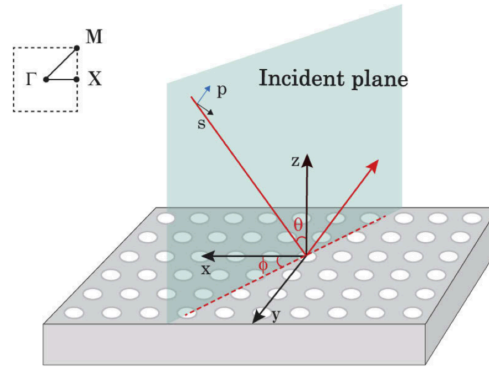


Figure 4.1. Configuration of the incident plane wave. The tilt angle from the normal (z) direction and the azimuthal angle from the x axis are denoted by θ and ϕ , respectively. The polarization of the incident wave is denoted by p (s) when its electric field is parallel (perpendicular) to the incident plane. The inset shows the first Brillouin zone of the 2D square lattice.

4.2.3 Theory

Finite-element calculations are carried out to determine the target PC design, that is, a 2D square lattice of (In, Ga)As cylindrical pillars with a height of $0.8 \mu\text{m}$, a radius of $0.565 \mu\text{m}$, and a lattice constant (a) of $1.365 \mu\text{m}$. This design results in a resonance between the measured QCL frequency and the second-lowest band edge at the Γ point ($\Gamma^{(2)}$) in the first Brillouin zone. (The $\Gamma^{(2)}$ originates from zone folding at the X symmetric point.) Here, the discussion is mainly dialed with the TM-like polarization modes, since a QCL employs intersubband electronic transitions, which have dipole moment perpendicular to the MQW layer.

Figure 4.2 is comparison between the vertical field distribution of the lowest TE-like mode ($TE^{(1)}$) and the second-lowest TE-like mode ($TE^{(2)}$). Fig. 4.2(a) shows the layer sequence of the sample and the refractive indices used for the calculation. Fig. 4.2(b) shows the field distribution of $TE^{(1)}$. It is strongly confined in the MQW layer along z axis, which is normal to the slab surface. Fig. 4.2(c) shows the field distribution of $TE^{(2)}$, which indicates a nodal distribution along the z axis. See the dispersion relation of $TE^{(1)}$ and $TE^{(2)}$ in Fig. 4.7(b) in the later text and the in-plane distribution of $TE^{(1)}$ in Fig. 4.3.

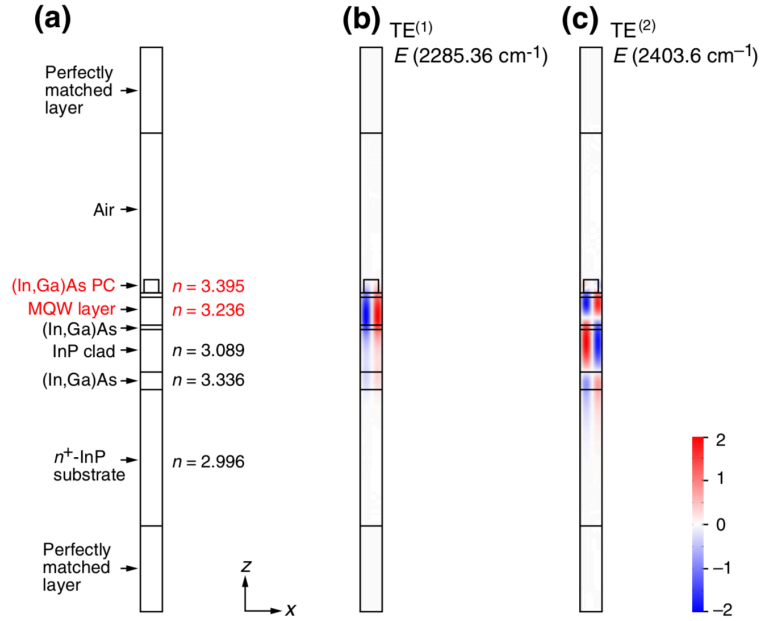


Figure 4.2. The vertical field distribution. (a) The layer sequence used for the calculation. Note that the z - axis is normal to the slab surface. The refractive index n of each layer is also indicated. The red-colored notations highlight the waveguide core region. (b), (c) The z component of magnetic field (H_z) for the lowest TE-like mode ($TE^{(1)}$) and the second-lowest TE-like mode ($TE^{(2)}$), respectively.

Figure 4.3 shows the in-plane magnetic field distribution of TE-like modes and Fig. 4.4 shows those of TM-like modes. All the in-plane distributions exhibit their peculiar symmetries, as can be seen in each panel.

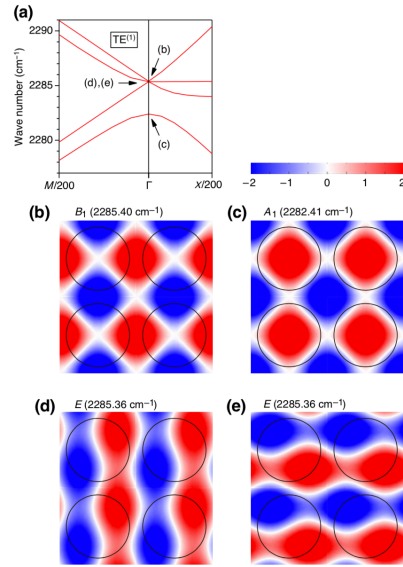


Figure 4.3. The in-plane field distribution for the TE⁽¹⁾ modes at the Γ point. (a) The dispersion relation in the vicinity of the Γ point. (b)–(e) The z component of magnetic field (H_z) for modes depicted by the arrows in (a). The black lines indicate the boundaries of circular pillars, which compose PC structures. All the in-plane distribution show their peculiar symmetries, which are characterized by (b) B_1 , (c) A_1 , and (d), (e) E for the C_{4v} symmetry. Note that the dispersion relation in (a) suggest the degeneracy of B_1 and E at the Γ - point and the formation of photonic Dirac cones [4.4–6], but in fact their eigenfrequencies are slightly different under the model condition.

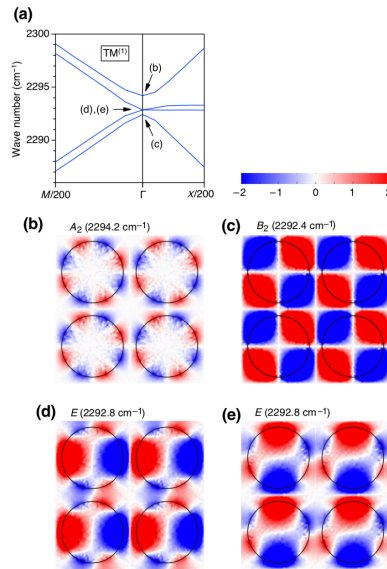


Figure 4.4. The in-plane field distribution for the TM⁽¹⁾ modes at the Γ point. (a) The dispersion relation in the vicinity of the Γ point. (b)–(e) The z component of magnetic field (H_z) for modes depicted by the arrows in (a). The black lines indicate the boundaries of circular pillars, which compose PC structures. Note that relatively large fluctuation of the image data is due to small H_z values for TM-like modes. Nevertheless, their spatial symmetries can be identified, which are characterized by (b) A_2 , (c) B_2 , and (d), (e) E for the C_{4v} symmetry.

4.3 Results and Discussions

4.3.1 Midinfrared characterization of PC slabs

Figure 4.5 shows reflection spectra at normal incidence ($\theta = 0^\circ$) for samples with different lattice constants. All the samples exhibit similar spectral curves, which shift to higher wave numbers (shorter wavelengths) in unison for smaller lattice constants. (The onset noisy spectra at 2320–2375 cm^{-1} , as shown by gray region, is due to light absorption by CO_2 .) The observed scaling behavior is evidence that signature spectra are induced by resonant coupling to PC modes.

The vertical arrows seen above each spectrum indicate the mode energies calculated using the finite-element method. The first and second arrows from the left (low-wave-number side) are the lowest-energy TE-like and TM-like modes, respectively. They are denoted by $\text{TE}^{(1)}$ and $\text{TM}^{(1)}$. The third and fourth arrows are higher-order confinement modes ($\text{TE}^{(2)}$ and $\text{TM}^{(2)}$), which have a nodal field distributions, see Fig. 4.5 in the Appendix). These calculated modes are in fairly good agreement with the measured spectral peaks, although the peak intensities are strongly dependent on the mode index, as discussed later. A discrepancy between the calculated and the measured energies is attributed to the use of inaccurate refractive indices for the constituent materials, particularly that of the bottom (In, Ga)As buffer layer, which contains relatively dense dopants and serves as an antiguiding plasmonic layer.

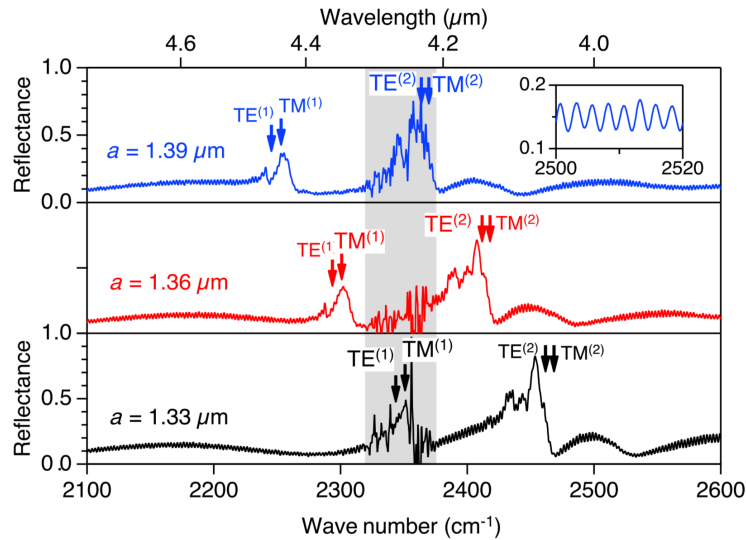


Figure 4.5. Normal incidence reflection spectra for samples with different lattice constants, $a = 1.33$, 1.36 , and $1.39 \mu\text{m}$. The gray region indicates a CO_2 absorption band, which causes clear spectral noises. The small sinusoidal modulation superimposed on spectra is due to Fabry-Perot interference between the top and bottom surfaces of the sample, as highlighted by the expanded spectrum in the inset.

Figure 4.6 shows a series of reflection spectra for various incident angles. Here, we study a sample where $a = 1.36 \mu\text{m}$ and analyze the spectra for both s- and p-polarization. In Figs. 4.6(a) and 4.6(b), from bottom to top, the incident beam is tilted from the surface normal toward the [100] in-plane axis, where the wave vector is moved from Γ to X in momentum space. For p-polarization [Fig. 4.6(a)] two intense peaks, which are classified as $\text{TM}^{(1)}$ and $\text{TM}^{(2)}$ at $\theta = 0^\circ$, are split into two peaks that move to the opposite side. Other small peaks classified as $\text{TE}^{(1)}$ and $\text{TE}^{(2)}$ stay almost constant. In contrast, for s-polarization [Fig. 4.2(b)], the intense peaks do not move but small split peaks, which originate from $\text{TE}^{(1)}$ and $\text{TE}^{(2)}$, are apparent at $\theta \gg 0^\circ$.

In Figures 4.6(c) and 4.6(d), the beam is tilted toward the [110] axis (45° away from [100]), and the wave vector is moved from Γ to M. In this geometry, all the peaks split and shift as the angle θ increases. Polarization dependence is not evident in these plots but the significant energy shift between s- and p-polarized spectra is analyzed. See also the spectral comparison in Fig. 4.8(a).

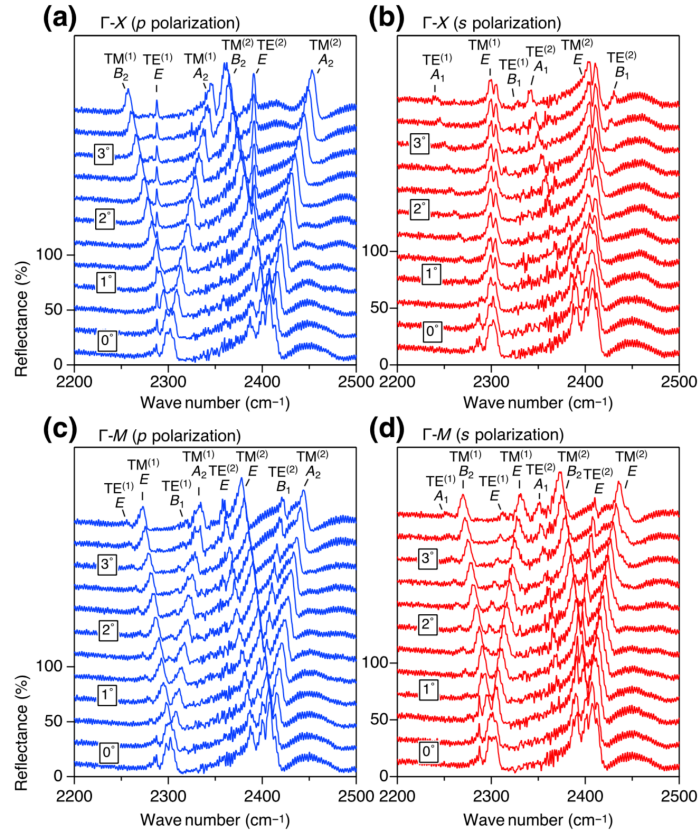


Figure 4.6. Angle-resolved reflection spectra for the sample where $a = 1.36 \mu\text{m}$. The spectra in each panel are arranged from bottom to top, $\theta = 0^\circ$ to approximately 3.7° in 0.35° steps. (a), (b) The p- and s-polarized spectra, respectively, where the incident beam is tilted inside a plain that contains the [100] axis of the square lattice. Accordingly, the wave vector moves along Γ -X axis in the first Brillouin zone.

(c), (d) The polarized spectra when the wave vector moves along Γ -M axis. The peak assignments are also indicated at the top in each panel.

4.3.2 Mode assignment and dispersion relations

These reflection peaks are assigned in term of irreducible representations of the C_{4v} point group [4.2]. For a uniform slab with no periodic modulation, the band edge at the $\Gamma^{(2)}$ point has fourfold degeneracy, which is then lifted into a doubly degenerate E mode and two other nondegenerate modes when the C_{4v} modulation is introduced into the slab. The nondegenerate modes are assigned to A_1 and B_1 for the TE-like modes and to A_2 and B_2 for the TM-like modes, where the symmetry operation of magnetic fields is considered. These mode symmetries are consistent with the prediction by group theory based on zone folding of TE and TM planar waveguide bands [4.2]. Of these modes, only the E mode is optically active at normal incidence, but the other modes are inactive due to symmetry mismatching. At off-normal incidence, all the modes become active and split. Group theory also predicts polarization-selection rules for the emergence of reflection peaks, which are described in Table 1 [4.7]. Using this table all the measured peaks can be safely identified. The assignment results can be seen at the top of each panel in Fig. 4.6. It is noteworthy that the above-mentioned symmetries are defined at the Γ point and the measured spectral peaks at finite incident angles do not necessarily follow the relevant symmetry characteristic.

Table 4.1. Selection rules for the observation of spectral peaks around the $\Gamma^{(2)}$ band edge in C_{4v} symmetric- PC slabs.

Mode symmetry ^a	Γ ($\theta = 0^\circ$)	Γ -X direction ($\phi = 0^\circ$)	Γ -M direction ($\phi = 45^\circ$)
A_1	inactive	s	s
A_2	inactive	p	p
B_1	inactive	s	p
B_2	inactive	p	s
E	active	s, p	s, p

^aThese mode symmetries are defined with the symmetry operation of magnetic fields.

The center energies of reflection peaks are evaluated via fitting. For simplicity, a multiple Gaussian function is used as a fitting model. The extracted energies for different θ values are summarized in the band-dispersion curves in Fig. 4.7(a), where spectral peak energies (in

wave-number units) are plotted as a function of a wave-vector projection to the slab plane, i.e., $(2\pi/\lambda) \cdot \sin \theta$, where λ is the vacuum wavelength. For comparison, Fig. 4.7(b) shows calculated band-dispersion curves over 1/50 of the first Brillouin zone. Both the measured and calculated curves agree well. Moreover, the field distribution of each mode is analyzed and that their symmetry agrees with the mode assignment based on selection rules is confirmed (see Figs. 4.3 and 4.4 and the related discussion as aforementioned above. Thus, angle-resolved reflection measurement is useful technique for experimentally determining photonic band structures.

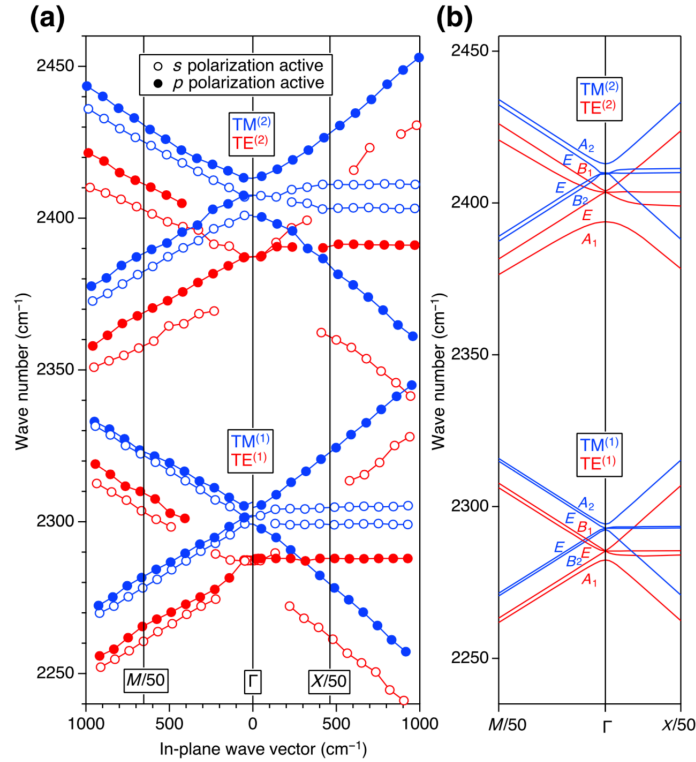


Figure 4.7. Dispersion relations based on measured angle-resolved reflection spectra in Fig 4.6.

(b) Calculated 2D dispersion relations, where it is assumed that $a = 1.365 \mu\text{m}$. The abscissa is normalized to 1/50 of the wave vector at the X-band edge ($\pi/50a$) and the M-band edge ($\sqrt{2}(\pi/50a)$).

4.3.3 Q-factor quantification

Figure 4.8(a) compares reflection spectra at $\theta = 3.7^\circ$ for different geometries and polarizations, the discussion is focused on the $\text{TE}^{(1)}$ and $\text{TM}^{(1)}$ frequency regions. The vertical lines indicate the assigned peak energies, which are determined by fitting. The spectra indicate a strong intensity dependence on the mode index (reflection peaks of different modes have different intensities). It can be speculated that the peak intensity is related to the mode coupling strength and thus the inverse of the Q factor, i.e., the rate of energy leakage from the waveguide. The following consideration supports the validity of this speculation.

A rigorous spectral analysis of 2D PC systems proves that the phase of electromagnetic waves transmitted through a PC slab is shifted by π across the resonance frequency [4.8]. Accordingly, the transmittance $|T|^2$ goes to zero at resonance and the reflectance $|R|^2$ goes to unity, since $|R|^2 = 1 - |T|^2$ for PC slabs made of nonabsorbing materials. Thus, the area (the spectrally integrated intensity) of the reflection peaks roughly scales with the spectral width $\propto Q^{-1}$ independent of other factors, although the exact spectral shape is rather complicated due to interference between the resonant spectral component and non-resonant backgrounds. In reality, the ideally sharp spectral structures are masked due to the influence of PC inhomogeneities and distributed angles of incidence. Nevertheless, it can be assumed that the peak areas are inversely proportional to the mode Q factors.

Figure 4.8(b) shows the experimentally determined and theoretically obtained Q^{-1} values for all $TM^{(1)}$ and $TE^{(1)}$ modes at $\theta = 3.7^\circ$. For the experimental determination, a simple expression, namely, $Q^{-1} = (2/\pi)S/\omega_0$ is adopted, where S is the peak area, i.e., $\int |R|^2 d\omega$, and ω_0 is the mode frequency. The coefficient $(2/\pi)$ arises from the normalization factor of the Lorentzian function. The measured Q^{-1} values reveal a fairly good agreement with the theoretical Q^{-1} values, which is calculated using the finite-element method, even without the use of any adjustable parameters. Hence, the reflection peak intensity provides a useful measure that is equivalent to the mode Q factor, i.e., it constitutes key information for understanding lasing properties.

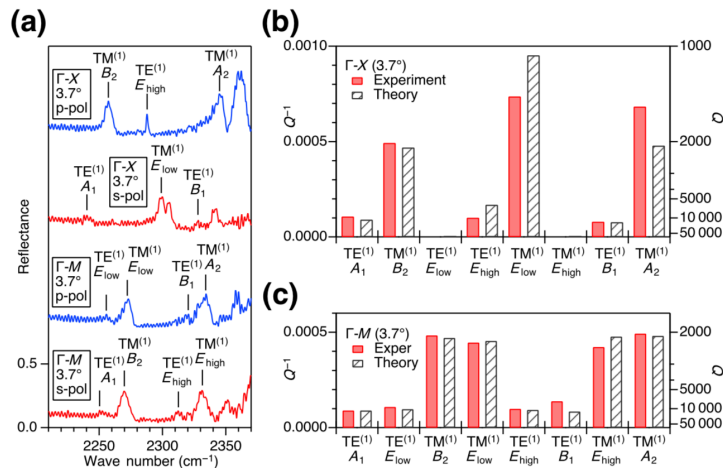


Figure 4.8. (a) Reflection spectra at $\theta = 3.7^\circ$ around the $TE^{(1)}$ and $TM^{(1)}$ frequency regions for different geometries and polarizations. The vertical lines indicate the mode center energies, which is determined via fitting. (b),(c) A comparison of the experimentally determined Q^{-1} values (red filled bars) and theoretically obtained Q^{-1} values (black hatched bars) for each mode depicted in (a) with (b) $\Gamma-X$ and (c) $\Gamma-M$ geometries. Note that the experimental Q^{-1} values are proportional to the areas of the reflection peaks.

Throughout this work, it is assumed that refractive indices are real numbers and ignore the impact of absorption loss on the mode Q factors. Hence, the Q^{-1} values, which are analyzed theoretically and experimentally, are governed purely by diffraction (radiation) loss. The Q^{-1} values are therefore equivalent to the rates of energy leakage from the waveguide to free space. To clarify the impact of material absorption on Q , they are calculated by using adequate complex refractive indices and the calculation results are shown in Table 4.2. They indicate that Q factors calculated using complex indices (Q_{total}) are significantly smaller than those calculated using real indices. The observed reduction Q_{total} is due to free carrier absorption, which is not negligible for QCL devices in the midinfrared region. Nevertheless, the present techniques based on angle-resolved reflection makes it possible to determine the output coupling strengths, which are generally non measurable if standard spectral techniques are used.

Table 4.2. A comparison of the Q factors calculated using real refractive indices and those calculated using complex refractive indices (Q_{total}) for each $\text{TE}^{(1)}$ and $\text{TM}^{(1)}$ mode at (a) $k = X/50$ along Γ -X direction and (b) $k = M/50$ along Γ -M direction. Note that the Q values calculated using real indices are used to plot Fig. 4.8(a) and 4.8(b).

	Wave number (cm^{-1})	Q (real n) ^a	Q_{total} (complex n) ^b
(a) Γ -X ($k = X/50$)			
$\text{TE}^{(1)}A_1$	2262.4	10968	2067
$\text{TM}^{(1)}B_2$	2270.9	2131	1131
$\text{TE}^{(1)}E$	2284.0	915694	2621
$\text{TE}^{(1)}E$	2285.5	5909	1788
$\text{TM}^{(1)}E$	2293.0	1050	743
$\text{TM}^{(1)}E$	2293.4	1064952	2489
$\text{TE}^{(1)}B_1$	2306.9	12718	2211
$\text{TM}^{(1)}A_2$	2315.3	2087	1155
(b) Γ -M ($k = M/50$)			
$\text{TE}^{(1)}A_1$	2261.8	11026	2079
$\text{TE}^{(1)}E$	2263.3	10241	2012
$\text{TM}^{(1)}B_2$	2270.5	2124	1147
$\text{TM}^{(1)}E$	2271.4	2198	1131
$\text{TE}^{(1)}E$	2306.2	10689	2136
$\text{TE}^{(1)}B_1$	2307.7	11701	2159
$\text{TM}^{(1)}E$	2314.9	2094	1174
$\text{TM}^{(1)}A_2$	2315.8	2078	1138

^aThe list of the real n values adopted for the calculation is shown in Fig. 4.2(a)

^bThe imaginary parts of the complex n values are estimated based on the doping levels of the QCL samples.

4.4 Conclusion

In conclusion, angle-resolved reflection measurement with using a Fourier-transform spectrometer is proposed as a useful technique to determine the in-plane dispersion relations of 2D PC slabs in the midinfrared region. All the complex PC modes are assigned by polarization analysis. The mode Q factors can be determined by using the peak intensity evaluation. Thus, the reflection measurement is useful for determining the optical conditions for PCSEL structures.

A potential problem inheres in the proposed technique is limited angular resolution and it might be rather difficult to distinguish fine-splitting spectra at the Γ point. However, the problem will be simply overcome by introducing a tunable external-cavity QCL as an excitation source, since it generates a near-plane-wave mid-IR beam. However, the frequency-tunable range is not so large. The adoption our Fourier spectrometer-based technique for broad spectral analysis and frequency-tunable QCLs for narrower spectral analysis should constitute a valuable approach for fully characterizing PC-slab samples that exhibit sharp resonance spectra.

References

- [4.1] T. Kuroda, S. Chalimah, Y. Yao, N. Ikeda, Y. Sugimoto, and K. Sakoda, "Apparatus for high-precision angle-resolved reflection spectroscopy in the mid-infrared region," *Appl. Spectrosc.* **75**, 259–264 (2021).
- [4.2] K. Sakoda, *Optical Properties of Photonic Crystals* (Springer-Verlag, Berlin, 2004), 2nd ed.
- [4.3] S. Saito, R. Hashimoto, K. Kaneko, T. Kakuno, Y. Yao, N. Ikeda, Y. Sugimoto, T. Mano, T. Kuroda, H. Tanimura, S. Takagi, and K. Sakoda, "Design and fabrication of photonic crystal resonators for single-mode ang vertical surface emission from strain-compensated quantum cascade lasers operating at 4.32 μm ," *Apply. Phys. Express* **14**, 102003 (2021).
- [4.4] X. Huang, Y. Lai, Z. H. Hang, H. Zheng and C. T. Chan, "Dirac cones induced by accidental degeneracy in photonic crystals and zero-refractive-index materials," *Nat. Mater.* **10**, 582–586 (2011).
- [4.5] K. Sakoda, "Proof of the universality of mode symmetries in creating photonic Dirac cones," *Opt. Express* **20**, 25181–25194 (2012).

- [4.6] S. Chalimah, Y. Yao, N. Ikeda, Y. Sugimoto, T. Mano, T. Kuroda and K. Sakoda, “Eigenmode symmetry assignment of triangular-lattice photonic crystal slabs and their Dirac cones materialized by effective degeneracy in the mid-infrared region,” *Opt. Express* **29**, 19486–19494 (2021).
- [4.7] Y. Yao, N. Ikeda, T. Kuroda, T. Mano, H. Koyama, Y. Sugimoto, and K. Sakoda, Mid-IR Dirac-cone dispersion relation materialized in SOI photonic crystal slabs, *Opt. Express*. **28**, 4194 (2020).
- [4.8] K. Ohtaka, Y. Suda, S. Sagano, T. Ueta, A. Imada, T. Koda, J. S. Bae, K. Mizuno, S. Yano and Y. Sagawa, “Photonic band effects in a two-dimensional array of dielectric spheres in the millimeter-wave region,” *Phys. Rev. B* **61**, 5267 (2000).

Chapter 5 Photonic crystal slabs with different pillar shapes and filling factors for application to photonic crystal surface-emitting quantum-cascade lasers

5.1 Introduction

In the last chapter, we focused on the square-lattice photonic crystal slabs with the perfect C_{4v} symmetry. However, in this case, only the E mode is optically active at normal incidence, and all the other modes are inactive due to symmetry mismatching. For light extraction from these modes, we need to design and fabricate a slightly asymmetric structure.

Here, we introduce various design concepts to creating ideal laser devices. We study square lattice PC slabs, which consist of nanopillars with different pillar shapes using angle-resolved reflection spectra [5.1]. Then, we clarify the mode dependence of the pillar shapes, and discuss the impact of filling factors on the coupling efficiency.

5.2 Methods

5.2.1 Design

In this work, PC slabs, which consist of a square lattice of nanopillars with different lateral shapes are studied. Fig. 5.1 shown a unit cell of PC slabs, which comprise circular, triangular, and pentagonal pillars. These pillars are $0.8 \mu\text{m}$ in height. Note that a square lattice PC slab with circular pillars has perfect C_{4v} symmetry. This high symmetry results in the partial mode degeneracy at the Γ point [5.2]. In contrast, the symmetry of PC slabs with triangular and pentagonal pillars is lower than C_{4v} . Thus, the mode degeneracy is fully lifted even at Γ point. Moreover, a PC slab with the pentagonal pillars has a filling factor (FF; ratio of the pillar cross-section to the unit cell area) that is larger than that with the triangular pillars. Hence the output coupling efficiency by changing the pillar shape can be controlled.

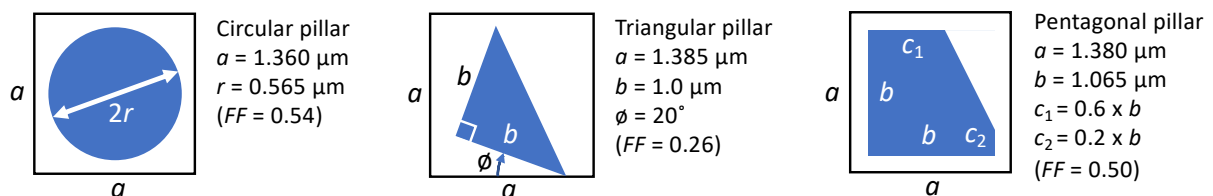


Figure 5.1. Unit cells of PC slabs, from left to right, with circular, triangular, and pentagonal pillars, where a is the lattice constant, r is the radius of the circular pillar, and FF is the filling factor. The other parameters are described in the figure annotations. All the pillars are $0.8 \mu\text{m}$ high.

5.2.2 Samples

QCL multilayer structures are grown on an InP substrate by molecular beam epitaxy. On the substrate, an InGaAs buffer layer, an InP bottom cladding layer, and a thin InGaAs guiding layer, followed by InGaAs/InAlAs strain-compensated multiple quantum well (MQW) with a total thickness $1.6 \mu\text{m}$ are grown. The MQWs serve as a QCL active layer that has an optical gain at a center wavelength around $4.4 \mu\text{m}$. Then a $1.0\text{-}\mu\text{m}$ -thick InGaAs, which is used for PC processing, is grown.

Before the microfabrication process, the output wavelength of each QCL wafer is measured, and a finite-element calculation is performed to determine PC structural parameters, which satisfy the resonant condition. In accordance with the optimal design, there-millimeter PC slabs are fabricated by using electron beam lithography and reactive-ion-beam etching techniques. Fig. 5.2 shows the top view of PC slabs with triangular and pentagonal pillars. They reveal that the target pillar shapes, shown in Fig. 5.1, are well reproduced in the fabricated devices.

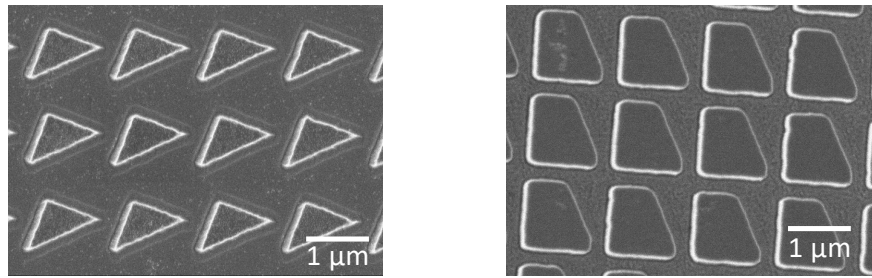


Figure 5.2. Scanning electron microscope images for PC slabs with triangular pillars ($a = 1.395 \mu\text{m}$, left), and pentagonal pillars ($a = 1.380 \mu\text{m}$, right). These pillars are periodically arranged to form square lattice crystals.

5.2.3 Optical measurement

Angle-dependent reflection spectra are measured with our home-made high-resolution setup, which is placed in the sample compartment of Fourier-transform infrared spectrometer (FTIR). A schematic diagram of the angle-dependent setup is shown in the Fig. 1.1 of Chapter 2, whose details is reported a recent publication [5.1]. In the setup, infrared light is carefully collimated with a parabolic mirror, and beam divergence is limited to less than 0.3° . The collimated beam passes through a beam splitter, which then transmits the beam from the sample to the detector. The setup enables to measure reflection spectra at normal incidence and to change the incident angle (θ) from -3.7° to $+3.7^\circ$ across zero.

The measurement configuration is shown in the Fig. 4.1 in Chapter 4. The tilt angle from the normal (z) direction and the azimuthal angle from the x -axis are denoted by θ and ϕ , respectively. Note that a change in the azimuthal angle between 0° and 45° allows to excite eigenmodes in the- Γ -X and Γ -M directions in momentum space, respectively.

5.3 Results and Discussions

5.3.1 Reflection spectra at normal incidence

Figure 5.3(a) shows reflection spectra at normal incidence for circular pillar slabs with different lattice constant [5.2]. All the spectra exhibit similar curves, which shift to higher wavenumbers (shorter wavelengths) in unison for smaller lattice constants. The observed size scaling behavior is evidence that signature spectra are induced by resonant coupling to PC modes.

The vertical lines seen in Fig. 5.3 each spectrum indicates the mode energies calculated using the finite-element method. The first and second lines from left (low-wave-number side) are the lowest energy TE-like (broken line) and TM-like (solid line) modes, respectively. The third and fourth lines are higher-order confinement modes, which have a nodal field distribution along the z -axis. These calculated modes are in fairly good agreement with the measured spectral peaks. The discrepancy between the calculated and measured mode energies is attributed to inaccurate refractive indices used in the numerical simulation.

The reflection spectra reveal the presence of the TE-like and TM-like modes, which are close to each other. The observed signature is in stark contrast to that for standard planar waveguides such as SOI and air-bridge PC slabs, where the splitting between the TE-like and the TM-like modes is generally much larger. The relatively small TE-TM splitting in the PC slabs is caused by the weak confinement of waveguide modes in the vertical direction, as a result of the small refractive index contrast. It is noteworthy that QCL works with TM polarizations as it employs intersubband electronic transitions, which have dipole moment perpendicular to the growth layer. (In contrast, standard interband semiconductor lasers work with TE polarizations.) Thus, the TM-like modes are considered to use as surface-emitting PC QCL resonators.

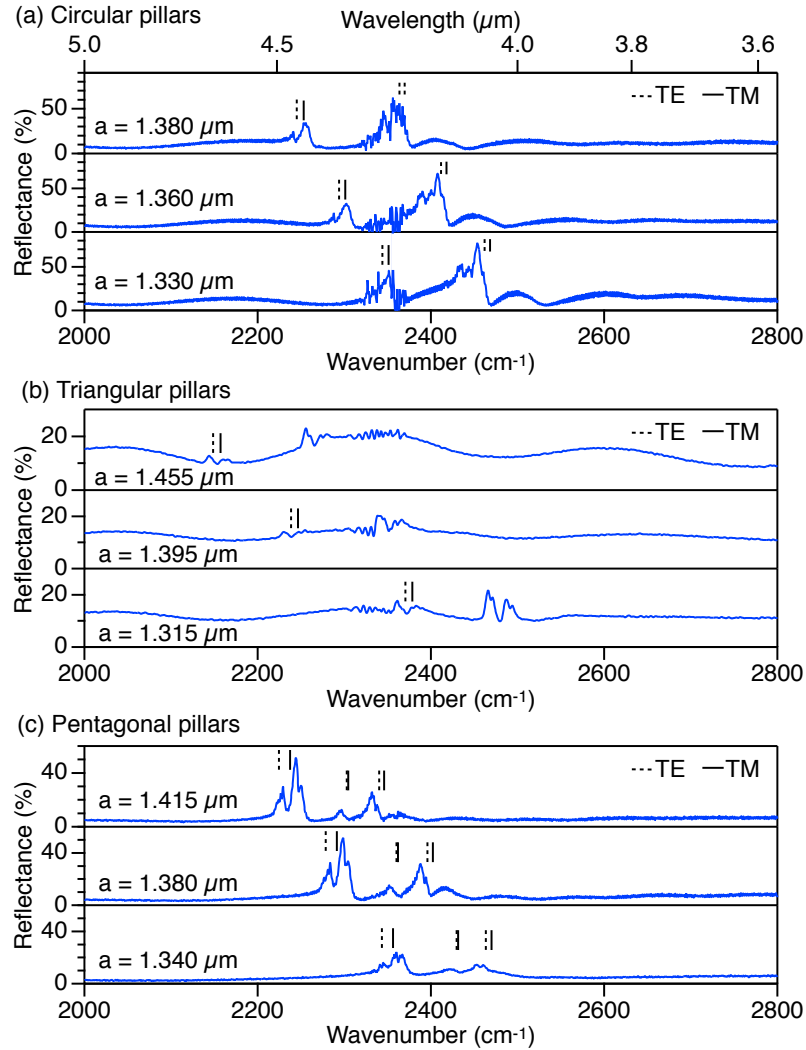


Figure 5.3. Normal incidence reflection spectra for PC slabs with (a) circular pillars, (b) triangular pillars, and (c) pentagonal pillars with three different lattice constants. The onset of noisy spectra at 2320–2375 cm⁻¹ is due to light absorption by CO₂. The broken and solid lines indicate the calculated TE-like and TM-like mode energies, respectively. The calculation is based on the finite-element method.

Figure 5.3(b) shows a series spectrum of the triangular pillar slabs. They reveal a spectral shift with lattice constant and a signature similar to that of the circular pillar slabs. However, the peak intensities are significantly lower than those of the circular pillar slabs. The observation of the small peak intensities implies a reduction in the mode coupling strength due to the small filling factor of the triangular pillar PCs (FF = 0.26 for the triangular pillars, and 0.54 for the circular pillars).

Figure 5.3(c) shows the spectra of the pentagonal pillar slabs. Here, the peak intensities have recovered to a reflectance value of around 50%, similar to those of the circular pillar slabs.

The high reflection intensities arise from the large effective index contrast thanks to the filling factor close to 0.5. The spectra exhibit several higher energy modes, whose field distributions indicate multiple nodes in the vertical direction.

Figure 5.4. compares the normal incidence spectra of the circular and pentagonal pillar slabs, where the discussion is focused on the lowest TE and TM frequency regions. The spectra of the circular pillar slab (Fig. 5.4(a)) consist of a small TE peak on the low energy side and a large TM peak on the high energy side. The two peaks shift together when the lattice constant is changed, as mentioned above.

The spectra of the pentagonal pillar slab (Fig. 5.4(b)) reveal a different signature. Each of the TE and TM peaks is asymmetric and likely consist of fine split lines. The Gaussian fitting result is plotted with the gray lines, where it is assumed that two Gaussians form the measured peak. Good reproducibility is found, which is suggested that each peak consists of two or more split peaks. The observed spectral splitting is related to the symmetry reduction in pentagonal pillar slabs, as discussed in the following.

For a uniform slab with no periodic index modulation, the band edge at the Γ point has a four-fold degeneracy, which is then lifted into a doubly degenerate E mode and two other nondegenerate modes when C_{4v} symmetric modulation is introduced into the slab. The nondegenerate modes are assigned to A_1 and B_1 for the TM-like mode, where the symmetry operation of electric fields is considered. Of these modes, only the E mode is optically active at normal incidence. The other modes are inactive due to symmetry mismatching. This is the case of PC slabs with circular pillars, which have a perfect C_{4v} symmetry. Thus, the measured peaks in Fig. 5.4(a) are assigned to the doubly degenerate E mode for both the TE-like and TM-like modes. For the pentagonal pillar slabs, the symmetry is slightly broken from C_{4v} , and all the modes become active and split. Hence, the emergence of up to four peaks in the spectra is expected, although just two of them are identified in Fig. 5.4(b) due to the limited resolution of the setup or the effect of sample inhomogeneities. The presence of multiple resonance peaks in normal incidence spectra is a preferable signature for the application of PC-slabs to surface-emitting lasers.

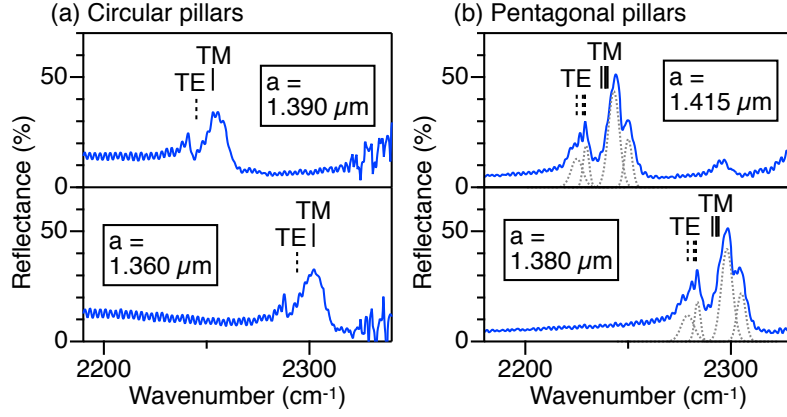


Figure 5.4. Normal-incidence reflection spectra in the energy region around the lowest TE-like and TM-like modes for PC slabs with (a) circular pillars, and (b) pentagonal pillars. The vertical lines indicate the calculated mode energies.

In Table 5.1, the calculated TM mode energies and Q factors, i.e., the effective time constant of energy leakage (in the unit of ω^{-1}) from waveguides into free space are calculated. The circular pillar slab has the B_1 , E, and A_1 modes at the Γ point. Of these modes, the B_1 mode is likely to achieve lasing as it has the largest Q value. However, the mode at the Γ point is not coupled to free space, and the laser light is not emitted along a direction normal to the surface. In contrast, the low symmetry pentagonal pillar slab has four split modes, all of which are coupled to free space. Thus, the highest Q mode leads to lasing, and generates efficient output in the surface normal direction.

Table 5.1. Calculated energies and Q factors for the lowest TM-like modes at the Γ point in the circular and pentagonal pillar slabs. In the calculation, complex refractive indices are adopted for the constituent materials, and take account of the effect absorption loss on the Q factors.

Circular pillar slab				
Wavenumber (cm^{-1})	2292.5		2292.9	2294.3
Q	2643		753	2295
Mode symmetry ^a	B_1		E (doubly degenerate)	A_1
Optical activity	inactive		active	inactive
Pentagonal pillar slab				
Wavenumber (cm^{-1})	2291.3	2292.9	2293.0	2294.3
Q	418	782	3176	3590
Optical activity	active	active	active	active

Note: The mode symmetry for the circular pillar slabs is determined by field distribution analysis [5.13].

5.3.2 Angle-resolved reflection spectra and dispersion relation

Figures 5.5 and 5.6 show a series of reflection spectra for various incident angles. Here, a PC slab with pentagonal pillars, where $a = 1.380 \mu\text{m}$ is studied and the spectra for both s- and p-polarizations are analyzed. In Fig. 5.5, from the bottom to top, the incident beam is tilted from the z-axis toward the [100] in-plane axis, where the wave vector is moved from Γ toward X momentum space. For p-polarization (left, blue lines), the intense TM-like modes at normal incidence are split into two peaks that move in the opposite direction at the angle θ increases. The weak TE-like modes stay almost constant. In contrast, for s-polarization (right, red lines) the intense TM-like modes do not move but the weak TE-like modes change into small split peaks $\theta > 0$. Thus, the TE-like and TM-like modes are found to have opposite polarization dependence.

In Fig. 5.6, the beam is tilted toward the [110] axis (45° away from [100]), and the wave vector is moved from Γ to M. In this geometry, all the peaks split and shift as the angle θ increases. Polarization dependence is not evident in these plots, but the significant energy shift between s- and p-polarized spectra are analyzed (not shown).

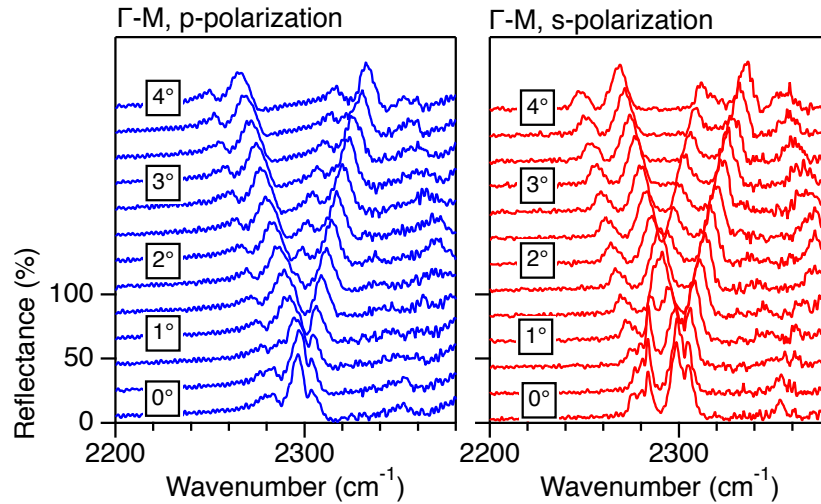


Figure 5.5. Angle-dependent reflection spectra for a pentagonal pillar slab with $a = 1.380 \mu\text{m}$. From bottom to the top, the incidence beam is tilted from z-axis towards the [100] in-plane axis with changing θ in 0.35° step. Accordingly, the wave vector moves in the Γ -X direction in momentum space. The left and right panels are p- and s-polarized spectra, respectively.

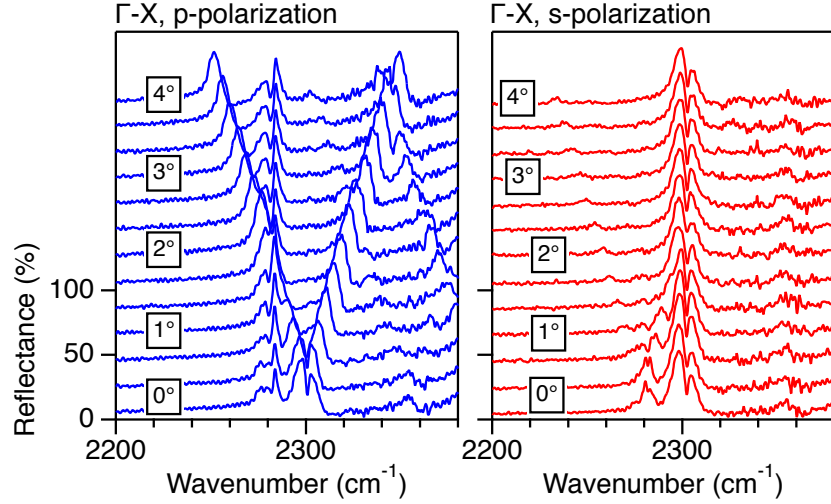


Figure 5.6. Angle-dependent reflection spectra for a pentagonal pillar slab with $a = 1.380 \mu\text{m}$, where the wave vector moves in the Γ -M direction in momentum space. The left and right panels are p- and s-polarized spectra, respectively.

The center energies of measured peaks are evaluated via fitting. For simplicity, a multiple Gaussian function is used as a fitting model. The extracted energy for different θ values is summarized in the band-dispersion curves in Fig. 5.7, where the spectral peak energies (in wavenumber units) are plotted as a function of wave vector projection to the slab plane, i.e., $(2\pi/\lambda) \sin \theta$, where λ is the vacuum wavelength. It reveals that, at finite k values ($k > 0$) in both the Γ -X and Γ -M directions, the measured split peaks are classified into four TE-like modes and four TM-like modes. With decreasing k , the four modes approach each other, as expected in square lattice PC slabs. However, the mode splitting remained even at $k = 0$ due to the broken symmetry of the pentagonal pillar slab.

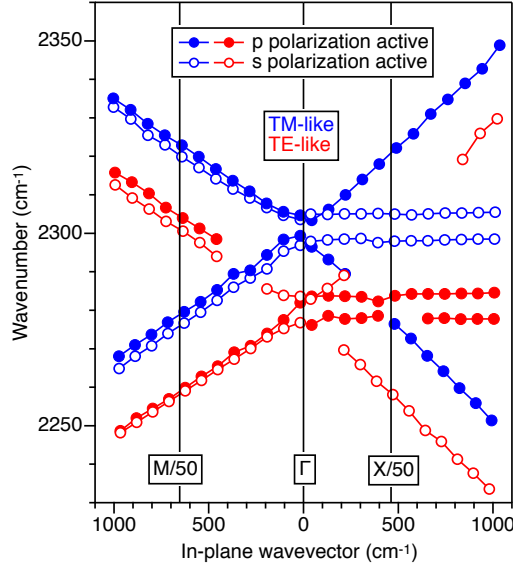


Figure 5.7. Dispersion relation based on measured angle-dependent reflection spectra in Figs. 5.5 and 5.6 for pentagonal slab with $a = 1.380 \mu\text{m}$. The two vertical lines indicate the wave vectors that correspond to 1/50 of the M and X symmetric points in the first Brillouin zone. The blue and red symbols are classified into the TM-like and TE-like modes, respectively. The filled circles are analyzed with p polarized spectra, and the open circles are analyzed with s polarized spectra. It is noteworthy that, in this dispersion plot the discussion is focused on the second-lowest photonic band edge at the Γ point, and this band edge originates from zone folding at the X point [5.4].

5.4 Conclusion

The application of photonic crystal slabs to QCL resonators is a powerful approach with which surface-emitting mid-infrared laser diodes are created. A prerequisite for surface normal emission is a perfect resonance between laser gain frequencies and in-plane waveguide modes at the Γ point. Thus, the mode characterization of PC slabs is a great importance, although it is difficult in the mid-infrared region when using standard techniques. Here, the measurement of normal incidence reflection spectra was proposed to verify the resonance condition. Moreover, the angle-dependent spectra map dispersion relation of PC slabs. The impact of the nanopillar shape on the mode characteristic was also clarified, and a way to optimize the resonator design was proposed. The measured spectra showed a good agreement with the predicted resonance peaks. Thus, our angle-resolved spectroscopy technique is useful for characterizing and further optimizing PC slabs for efficient mid-infrared surface emission.

References

- [5.1] T. Kuroda, S. Chalimah, Y. Yao, N. Ikeda, Y. Sugimoto, and K. Sakoda, “Apparatus for high-precision angle-resolved reflection spectroscopy in the mid-infrared region,” *Appl. Spectrosc.* **75**, 259–264 (2021).
- [5.2] S. Chalimah, Y. Yao, N. Ikeda, K. Kaneko, R. Hashimoto, T. Kakuno, S. Saito, T. Kuroda, Y. Sugimoto and K. Sakoda, “Midinfrared dispersion relations in InP-based photonic crystal slabs revealed by Fourier-transform angle-resolved reflection spectroscopy, *Phy. Rev. Appl.* **15**, 064076 (2021).
- [5.3] S. Saito, R. Hashimoto, K. Kaneko, T. Kakuno, Y. Yao, N. Ikeda, Y. Sugimoto, T. Mano, T. Kuroda, H. Tanimura, S. Takagi, and K. Sakoda, “Design and fabrication of photonic crystal resonators for single-mode ang vertical surface emission from strain-compensated quantum cascade lasers operating at 4.32 μm , *Apply. Phys. Express* **14**, 102003 (2021).
- [5.4] K. Sakoda, *Optical Properties of Photonic Crystals* (Springer-Verlag, Berlin, 2004), 2nd edn.

Chapter 6 Summary and outlook

In this PhD study, we developed a high-resolution angle-resolved reflection measurement technique in the midinfrared region and applied the technique to the study of silicon-on-insulator (SOI) PC slabs and actual PC-QCL devices formed of In(Ga,Al)As/InP multilayer structures. Here, we summarize our results, and then, propose future works.

In Chapter 2, we discuss our home-made optical setup to demonstrate a high-resolution angle-resolved reflection measurement in the midinfrared region. To obtain high-resolution measurement, we utilized a parabolic mirror to convert the focused beam from light source to an achromatically collimated beam passing through the sample. Thus, to estimate the high-angle resolution, we measured the reflection intensity of a silver mirror mounted on the sample holder as a function of rotation angle. The results show that the angle dispersion is as high as 0.25° . The result enables us to give the tunable range of the incident angle of around 8° . To verify the accuracy of our home-made setup, we obtained the identical spectra from a bulk PMMA measured by using our home-made setup at normal incidence ($\theta = 0^\circ$) and a commercially available variable-angle reflection accessory (Harrick Scientific, Seagull) at near normal incidence ($\theta = 4^\circ$).

We demonstrated our technique to measure the normal incidence reflection spectra of a SOI PC sample and SOI alone. The SOI PC sample shows various spectral peaks as a result of resonant coupling between the incident light and the waveguide modes. Since the wavevector of light at normal incidence does not have a projection onto the slab layer, the incident light is only coupled to the waveguide mode at the Γ point ($k_{\parallel} = 0$). Consequently, the small peaks represent the mode distribution at the Γ point as a function of frequency (band energy). We also compared the normal incidence reflection spectra of SOI sample measured using our optical setup and commercial setup. The resonance peaks in the square-lattice SOI PC samples were only clearly shown by our optical setup. Thus, we once again confirmed a high angle resolution of our setup.

Using our home-made optical setup, we investigated the reflection spectra with different incident angles for square-lattice SOI PC samples with different radii and exhibited the signature of an optical phenomenon, i.e., Dirac cone formed at the Γ point. As aforementioned above, in midinfrared lasing application, it is expected that our home-made optical setup is useful to identify the in-plane waveguide dispersion.

In Chapter 3, we conducted angle-resolved reflection measurements in SOI triangular-lattice photonic crystal slabs with different air holes, $r = 530$ and 560 nm. SOI PC slabs have

a high refractive index contrast. Thus, TE-like and TM-like modes are larger further apart from each other. For each PC slab, we concentrated on observing the lowest TE mode which is folded into the first Brillouin zone with the second smallest reciprocal lattice. One peak with a broad spectral width is active attributed to E_1 -symmetric eigenmode at a normal incidence. This peak shift and several peaks appear as a result of the increasing incident angles. Then, we revealed eigenmodes in band structures along Γ -K ($\phi = 0^\circ$) and Γ -M ($\phi = 90^\circ$) directions for both s-and p-polarizations. In our investigation, we confirmed the existence of E_1 -, E_2 -, A_1 -, and B_1 -symmetric modes. In addition, we observed an exceptional mode, i.e., A_2 -symmetric mode which originates from the zone-folding of a transverse magnetic TM waveguide mode by the smallest reciprocal lattice. A previous study reported that through $\mathbf{k}\cdot\mathbf{p}$ perturbation method, distorted Dirac cone (linear dispersion) was produced by the accidental degeneracy of an E_1 -symmetric mode and an A_1 -/ A_2 -symmetric mode in the vicinity of the Γ point. When the E_1 -mode has a small quality vector, the linear dispersion is deviated and an exceptional point identifies its dispersion. The redistribution of the diffraction loss is induced by the mixture of the E_1 -symmetric mode and an A_1 -/ A_2 -symmetric mode. As a result, the width of the two peaks of Dirac cone is identical, which is one half of the original width of the E_1 -symmetric mode. From our PC slab that was designed to produce Dirac cone, we did not identify accidental degeneracy with the E_1 -symmetric mode. However, we found that the spectral width of A_1 -origin mode at $\theta = 4^\circ$ is approximately one half compared to the E_1 -symmetric mode. Thus, through-this investigation, we concluded that Dirac cone is materialized by effective degeneracy and has a good agreement with the theoretical study.

In Chapter 4, we studied the angle-resolved reflection spectra of square-lattice PC slabs with circular pillars in actual PC-QCL devices. The PC slabs own a low refractive index contrast that makes the TE-like-energy and TM-like-energy modes are close to each other. QCL has intersubband transition and TM polarization. We identified the first- and second-lowest TE-like ($TE^{(1)}$ and $TE^{(2)}$) and TM-like ($TM^{(1)}$ and $TM^{(2)}$) modes. We compared the normal incidence reflection spectra for samples with three different lattice constants, $a = 1.33$, 1.36 , and $1.39 \mu\text{m}$. All PC slabs show similar spectral curves, which shift to higher wave numbers (shorter wavelength) in unison for smaller lattice constants. Thus, we studied a series of reflection spectra for various incident angles in the PC slabs with $a = 1.36 \mu\text{m}$ which is designed emit a targeted-wavelength source. The measurements were applied toward Γ -X ($\phi = 0^\circ$) and Γ -M ($\phi = 45^\circ$) directions for both s-and p-polarizations. We assign the mode assignments to the reflection peaks based on the irreducible representation of the C_{4v} point

group with the symmetry operation of-magnetic fields, i.e., a doubly degenerate E mode and two other nondegenerate modes (A_1 and B_1 for the TE-like modes and to A_2 and B_2 for the TM-like modes). For the PC slabs with circular pillars, when the doubly degenerate E mode is active at normal incident, the other two modes are inactive due to symmetry mismatching. Therefore, in the lasing action, the two other modes cannot emit light outside the PC slabs. Afterwards, we summarized our spectral peak energies which are plotted as a function of waves in photonic band structures. Here, we also determined a fundamental parameter for laser action, namely the quality (Q) factors by using the peak intensity evaluation.

Chapter 6 discusses the reflection spectra in PC slabs in actual PC-QCL devices with different pillar shapes and filling factors (FF). First, we assigned the spectral peak of the first- and the second lowest energy TE-like and TM-like modes and then compared the peak intensities of the normal reflection incidence in PC slabs with high symmetry of the C_{4v} point group (circular pillar) and a lower symmetry than C_{4v} (triangular and pentagonal pillars). Because of a smaller FF, we observed that the triangular pillars slabs have lower peak intensities comparing with circular pillar slabs (FF= 0.26 for the triangular pillars, and 0.54 for the circular pillars). In pentagonal pillar slabs, when its FF is around 0.5, the peak intensities tend to show a similar value to the circular pillar slabs. At a normal incidence of each TE and TM mode, the reflection spectra of the pentagonal pillar slabs exhibit two or more splitting peaks because of their symmetry reduction. Our experimental results only classified two spectral peaks among the emergence of up to four peaks that we expected from the theoretical study. With these results, we expect that PC slabs with pentagonal pillars will have the highest emission efficiency.

To summarize, we successfully revealed photonic band structures at the vicinity of the Γ point by using our high-resolution angle-resolved reflection measurements. We found that our technique could be used to assign eigen symmetry of TE-like and TM-like modes in SOI triangular- and InP square-lattice PC slabs which own a high refractive index contrast and a low refractive index contrast, respectively. Moreover, we clarified a fascinating phenomenon, i.e., Dirac cone materialized by effective degeneracy in the midinfrared regions on the triangular-lattice PC slab. Thus, I believe our technique will be useful to identify many other optical phenomena in the midinfrared regions in the future.

For the future work, we plan to develop our PC-QCL devices for gas sensing application.

Acknowledgement

I would like to thank all people who have supported and helped me directly or indirectly during my PhD study and the research thesis in Japan.

First and foremost, I would like to express my sincerest gratitude and appreciation to my supervisor, Prof. Takashi Kuroda, for giving me the opportunity to join Kyushu-NIMS graduate assistantship program since April 2019. He clearly has taught me how to understand and to improve my knowledge in this research field. I am grateful for his uncountable time in abundant discussion, valuable advice, continues encouragement, and motivation with this research, publications, and thesis. He is my role model as a good researcher who always works hard, disciplinary, professionally, responsibly, and honestly.

I deeply thank all the members of our research project, particularly Prof. Kazuaki Sakoda and Dr. Yuanzhao Yao for their kind help and support. They taught me theoretical aspects of this study. They also helped me for the preparation of papers and conference talks. I would like to express my sincere gratitude to Prof. Yoshimasa Sugimoto, Dr. Naoki Ikeda, Dr. Takaaki Mano, and collaborators from Toshiba Corporation (Dr. Kei Kaneko, Dr. Rei Hashimoto, Dr. Tsutomu Kakuno, and Dr. Shinji Saito) for providing me the samples which have been a very crucial part of this research work.

I thank Professors Tsuyohiko Fujigaya and Chihaya Adachi for their time and valuable comments for completing my thesis.

My special thanks to all colleagues and friends of mine, Efi, Viola, Maya, my office's friend, Ha-san, and many others that I can mention one by one for their encouragement throughout my PhD study. I would like to express my deepest love and thank to my parents, younger brothers (Najib, Zain, and Farid), and younger sisters (Solik, Amid, and Nabila).

Finally, all praises to Allah, my God, the Entirely Merciful and Especially Merciful, for all blessing and giving me strength during hard time.

August 2022